Growth and evolution of long-lived, large volcanic clusters in the Central Andes: the Chachani Volcano Cluster, southern Peru

Rigoberto Aguilar[1], Jean-Claude Thouret[2], Pablo Samaniego[2], Gerhard Wörner[3], Brian Jicha[4], Jean-Louis Paquette[2], Edwin Suaña[5], Anthony Finizola[6,7]

[1] Observatorio Vulcanológico del INGEMMET, Dirección de Geología Ambiental y Riesgo Geológico, Urb. Magisterial 2 B-16, Yanahuara, Arequipa, Perú (raguilar@ingemmet.gob.pe)

[2] Université Clermont Auvergne, Laboratoire Magmas et Volcans UMR 6524 CNRS, OPGC, IRD, Campus Universitaire des Cézeaux, 6 Avenue Blaise Pascal, 63178 Aubière Cedex, France (j-claude.thouret@uca.fr, pablo.samaniego@ird.fr; j-louis.paquette@uca.fr)

[3] Georg-August Universität, Abteilung Geochemie, Goldschmittstraße 1, Göttingen, 37077, Germany (gwoerne@gwdg.de)

[4] Department of Geosciences, University of Wisconsin, Madison 1215 West Dayton Street Madison, WI, 53706, USA (brian.jicha@wisc.edu)

[5] Universidad Nacional San Agustín, Facultad de Ingeniería Geológica, Geofísica y Minas, Arequipa, Perú (yuve04@gmail.com)

[6] Université de La Réunion, Laboratoire GeoSciences Réunion, F-97744 Saint-Denis, France (anthony.finizola@univ-reunion.fr)

[7] Université de Paris, Institut de physique du globe de Paris, CNRS, F-75005 Paris, France

Abstract

In the Central Andes, large (> 500 km^2) and long-lived (1-5 Ma) volcanic clusters (LVCs) are less explored and their eruptive history and magmatic regimes less understood than smaller, short-lived (<0.5 Ma), individual stratocones. The Chachani-large volcanic cluster (C-LVC) sizeable volume (*c.* 290 km^3) consists of twelve edifices forming the 1.06 - 0.64 Ma group of stratovolcanoes and the 0.46 - 0.05 Ma group of domes coulees and block-lava flow fields. Both groups overlie pre-Chachani lavas and tuffs 1.02-1.27 Ma, and together they have buried large nested craters or a caldera associated with the *c.* 1.62-1.66 Ma Arequipa Airport ignimbrite. The C-LVC evolved from: (i) homogeneous compositions of the pre-Chachani and Chachani basal eruptive units to (ii) relatively wide compositional variations (53-67 wt.% SiO_2) between mafic andesite and dacite at moderate eruptive rates (0.27 - 0.41 km^3/ka) for the 'Old Edifice' group, and finally to (iii) narrower (57-64 wt.% SiO_2) andesitic compositions coinciding with extrusive activity at 2.5 times lower eruptive rates (0.12 - 0.15 km^3/ka) for the 'Young Edifice' group. The large compositional variations in the Old Edifice group are related to strongly contrasting resident and recharge magma compositions of hybridized lavas. In contrast, the narrow compositional range and lower eruption rate during the second half of the C-LVC eruptive history represent a trend towards more homogeneous, andesitic magma composition with time. Mineral texture and compositional studies provide evidence for disequilibrium and magma mixing in the C-LVC shallow (5-20 km depth range) magma reservoirs. These temporal changes in magma composition document that the transcrustal magma systems of the C-LVC evolved and matured with time by a combination of processes: fractional crystallization, crustal contamination and magma mixing/mingling with variable rates of mafic recharge. This resulted in a shift in time to a steady state, monotonous (andesite) regime as a result of coupling between compositional parameters and thermal conditions, density constraints, and the viscosity/crystallinity of erupted magmas.

Keywords: volcanic cluster, petrogenesis, eruptive rate, Chachani, Central Andes, Peru

1. INTRODUCTION

The Central Volcanic Zone (CVZ) of the Andes is an excellent natural laboratory in which the interactions between magma genesis and crustal evolution can be explored (e.g., Wörner et al., 2018). These interactions have led to four main constructional volcanic types: (1) andesitic and dacitic composite stratovolcanoes, (2) large volcanic clusters (LVCs) that have erupted relatively wide compositional ranges from mafic andesites to dacites, (3) voluminous rhyodacitic ignimbrite fields, and (4) scarce, volumetrically insignificant, basaltic or basaltic andesitic, monogenic fields.

Studies of individual composite volcanoes in the Andean CVZ over the past 30 years have provided a fundamental understanding of the eruptive behavior, timescales and magmatic evolution needed to explain the variability of erupted lavas (e.g., Wörner et al., 1988; Davidson et al., 1990, 1991; Feeley et al., 1993, 1994; Mathews et al., 1994; Gardeweg et al., 1998; Thouret et al., 2001, 2002, 2005, 2007; Gerbe and Thouret, 2004; Clavero et al, 2004; Delacour et al., 2007; Harpel et al., 2011; Walker et al., 2013; Godoy et al., 2014; Rivera et al., 2014, 2017; Samaniego et al., 2016; Wörner et al., 2018; Samaniego et al., 2020; Mariño et al., 2021). By contrast, there are few studies on the eruptive and compositional history and thermal evolution of long-lived volcanic clusters (> 1 Ma), such as the Aucanquilcha volcanic cluster (Grunder et al., 2008; Klemetti and Grunder, 2007; Walker et al., 2013), Taápaca in northern Chile (Clavero et al., 2004; Rout and Wörner, 2021), and the Nevado Chachani and Nevado Coropuna clusters in southern Peru (Table 1).

From petrological and geochemical studies at a regional scale, three end-member magmas dominate andesite formation in the CVZ: calc-alkaline basaltic andesite, Sr-enriched basalt, and rhyodacite (Blum-Oeste and Wörner, 2016). Highly evolved, rhyolitic magmas (>72 wt.% SiO_2) rarely erupt in the CVZ from stratovolcanoes or domes; only limited rhyodacite eruptive centers are found in SW Peru, such as the Purupurini dome cluster (Bromley et al., 2019), the *c.* 34 ka-old pyroclastic deposits of El Misti cone (Thouret et al., 2001; Rivera et al., 2017) and the 25-9.7 ka caldera-related Plinian tephra-fall deposits of Ubinas cone (Thouret et al., 2005; Samaniego et al., 2020). Wörner et al. (2018, their Fig. 7) proposed the concept of different magmatic regimes in transcrustal magma systems to better understand the variability of volcano types in the Central Andes. Increasing recharge rates and decreasing volcano lifetimes characterize three distinct regimes feeding CVZ polygenetic volcanoes, including: (1) long lived (several My) clusters that evolve slowly from varied magmatic compositions to mostly uniform dacitic lavas (e.g., Aucanquilcha cluster); (2) stratovolcanoes constructed from

93 products with a large compositional range over a short period of time (a few hundred kyr, e.g.,
94 El Misti, Ubinas, Ampato-Sabancaya), and; (3), fast growing, short-lived stratocones (e.g., 10
95 kyr "Young Cone Parinacota") with monotonous andesitic composition. Wörner et al. (2018)
96 proposed that magmatic regimes can evolve, but also change back and forth from one end-
97 member to the other depending on the rate of recharge of hotter, less evolved magmas from
98 below and the size and temperature of resident, evolved magmas at shallow levels, i.e., between
99 *c.* 5 and 20 km in the upper crust. Albeit less active than iconic stratovolcanoes, LVC belie a
100 rich history of eruptive styles and epitomize the evolution of the magmatic regimes in the
101 Andean CVZ. As LVC magmas originated from depth and crossed shallow reservoirs in the
102 upper crust, unraveling the temporal changes in volume, eruption rate, and composition can
103 provide relevant information about protracted, productive transcrustal magmatic systems in the
104 Peruvian CVZ.

105 The Chachani large volcanic cluster (C-LVC) illustrates the shift between magmatic regimes
106 through its *ca.* 1.27 Myr lifetime: a relatively large compositional range from mafic andesites
107 to dacites at a moderate eruptive rate, followed by homogeneous andesitic magmas emplaced
108 by eruptive rate 2.5 times slower, i.e., 0.12-0.15 km^3/ka *versus* 0.27-0.41 km^3/ka (Tables 1-4
109 and section 8.2). C-LVC may be compared with other LVCs such as Coropuna in southern Peru
110 because both developed shortly after the eruption of ignimbrites of substantial volume (20–50
111 km^3) of Early Quaternary age (*c.* 1.66–1.28 Ma) with outflow sheets underlying both LVC's.
112 Paleomagnetic measurements point to sources likely located below these clusters (Paquereau-
113 Lebti et al., 2008; Thouret et al., 2017; Mariño et al., 2020). We document in detail the
114 stratigraphic sequence and construction of the Chachani large volcanic cluster based on
115 analyzed magmatic compositions and new $^{40}Ar/^{39}Ar$ ages. We further propose the links between
116 this LVC and preceding medium-sized ignimbrites as a generic pattern of magma evolution in
117 LVC's in general.

118

119 ## 2. LVC DEFINITION AND THE CHACHANI CASE STUDY

120 ### 2.1. LVC definition and differences from other CVZ polygenetic volcanoes

121 Large volcano clusters (LVCs) are the most voluminous constructional landforms amongst the
122 broad category of polygenetic volcanoes (Table 1) next to composite stratocones and compound
123 volcanoes (Francis, 1993; Grosse et al., 2009, 2013). A LVC is defined as an extensive (250-
124 700 km^2) and voluminous (200-600 km^3) assemblage of spatially, temporally and genetically

125 related, clustered volcanic edifices and eruptive centers. It comprises composite and compound
126 cones with associated lava flows and pyroclastic deposits, overlapping dome complexes and
127 their coulees, as well as fissure-fed, lava-flow fields (Francis, 1993). As such, LVCs are larger
128 than typical symmetric stratocones in the CVZ (≤ 140 km^2, e.g., El Misti, Parinacota; Table 1)
129 or compound volcanoes (≤ 200 km^2, e.g., Ampato-Sabancaya, Taápaca; Table 1).

130 LVC's also remain active over a long (> 1 Ma) period, roughly twice as long than the growth
131 period of typical individual composite or compound volcanoes (e.g., Hildreth and Lanphere,
132 1994; Hildreth et al., 2003; Singer et al., 1997; Coombs and Jicha, 2021; Table 1).
133 Exceptionally, the eruptive activity of an LVC may extend in the same area over as much as 11
134 Ma as in the case of the Aucanquilcha cluster (Klemetti and Grunder, 2007; Grunder et al.,
135 2008; Table 1). Beyond size and extended periods of activity, we argue that LVC's in the
136 Central Andes are specific in that they typically overly medium-sized ignimbrite-deposits. The
137 field and lithological relations indicate that pulses of silicic ignimbrite-forming magmas are
138 followed by slow "bleeding" of magmas with a variable range in composition from silicic to
139 mafic, again followed by a regime of more uniform hybrid intermediate andesite flows and
140 domes. So, its volume, lifetime, and the overall evolution of the magmatic regimes, distinguish
141 LVC's from other large volcanic complexes (Table 1).

142 **2.2. Structure and landform of the Chachani large volcanic cluster**

143 Extending 28.5 km from N to S and 22.5 km from W to E, the C-LVC is one of the largest
144 Andean CVZ volcanic clusters with an area of nearly 600 km^2 and an estimated maximum bulk
145 volume of 290 - 350 km^3 ± 10% (Fig. 1, Tables 1 and 3**,** see Sections 4.1 and 8.1). The present
146 summit of the Chachani Volcanic Cluster at 6073 m asl is formed by the highest, and youngest
147 snow-capped 'Nevado Chachani' stratovolcano (*c.* 0.131 Ma) located 22.5-km NNW of
148 downtown Arequipa and only *c.*15 km WNW of summit of El Misti volcano. The older volcanic
149 edifices include five more compound and composite cones, five cumulo-domes (dome
150 complexes), and widespread compound aa- and block-lava fields. The abundance of andesitic
151 lava flows and scarcity of more evolved rhyodacitic to rhyolitic pyroclastic deposits is a LVC
152 feature that has already been highlighted for the Aucanquilcha cluster (Klemetti and Grunder,
153 2007).

154 This large group of at least twelve individual edifices makes the C-LVC distinct from typical
155 and widely occurring individual stratocones (e.g., El Misti, Ubinas, Fig. 1) and from compound
156 volcanoes (e.g., Ampato-Sabancaya, Samaniego et al., 2016; Taápaca, Clavero et al., 2004;

Rout and Wörner, 2021) in the central Andes. Specifically, we emphasize three distinguishing characteristics: (1) The large size (average basal diameter 25 km, 3 to 3.6 km total height above the basement) and volume of the C-LVC exceed three- to sixfold that of typical CVZ composite volcanoes (40-65 km^3), including compound volcanoes (60-100 km^3: Table 1, and references therein). This is accentuated by a wider comparison of conically shaped CVZ stratovolcanoes to the LVC made by Karátson et al. (2012), who calculated a median of 69.1 km^3 for the present volume of 33 Neogene to Quaternary volcanoes in the CVZ, increasing to 88.9 km^3 after correction for erosion. Nine examples from their compilation exceed 100 km^3, and the reconstructed volume yielded 200 km^3 for only three of them. Therefore, because stratovolcanoes rarely exceed 200 km^3, LVCs can be defined as the most voluminous volcanic edifices in the central Andes (not counting, of course, large caldera complexes, de Silva and Kay, 1988), e.g., C-LVC and Coropuna LVC. Magmas emplaced in the CVZ must ascend and interact with a thick crust, becoming evolved, mixed and crystal-rich making difficult the formation of very large stratovolcanoes/compound volcanoes as in the other volcanic settings over thin crust and with an extensional tectonic regime (such as Alney-Chashakondzha in Kamchatka, 207 km^3; Grosse et al., 2014). Should erosion be accounted for, the initial volume of C-LVC would increase by as much as 15%, that is to e.g., 333 - 397 km^3 (see section 8.1). (2) The *c.*1.27 My duration of volcanic activity of C-LVC indicates that its longevity is twice to three times that of the CVZ individual composite volcanoes (Table 1, and references therein); (3) Simple and compound composite cones of different age, overlapping each other, suggest that eruptive activity has migrated to form two main alignments, firstly N120°E-trending over *c.* 9 km for the Old Edifice group and secondly 80°E-trending over 7.5 km for the 'Young Edifice' group. Such migration is out of proportion compared to flank eruptions feeding small edifices at individual stratovolcanoes.

Thus, while eruptive volumes, migration of eruptive activity and longevity of LVC's are different, their compositional range from medium to high-K, calc-alkaline basaltic andesite to dacite is similar to the typical compositional range of most stratovolcanoes in the CVZ. However, their size and lifetime differ, and this must reflect different rates and conditions of magma processing and focus on the function of transcrustal magma systems that are feeding these LVCs in the CVZ.

3. GEOLOGICAL AND TECTONIC SETTING

3.1. Regional geologic setting

The C-LVC of Pleistocene age (≤ 1.27 Ma) belongs to the active volcanic front of subduction-related volcanism in the Central Andes. It is built upon older (2.60-1.30 Ma) volcanic rocks (Fig. 2) of the Early Quaternary volcanic arc (Tosdal et al., 1981; James, 1982; James and Sacks, 1999; Thouret et al., 2016). The pre-volcanic basement under C-LVC and around the Arequipa depression consists of two large magmatic domains, the Atico-Mollendo-Tacna Domain (Coastal Batholith), and the Western Cordillera, which are separated by the Cincha-Lluta-Incapuquio fault system (Fig. 3A; Vicente et al., 1982; Benavides-Caceres, 1999; Ramos, 2008, 2010; Carlotto et al., 2009). The Western Cordillera is formed by Neogene volcanic deposits, according to the Peruvian stratigraphic nomenclature: Tacaza Group (Oligocene), Huaylillas Formation (Miocene) and Barroso (Plio-Quaternary) Group (for a more detailed chronostratigraphy, see Mamani et al., 2010 and Thouret et al., 2016, 2017). These volcanic and sub-intrusive units cover Jurassic sediments of the Yura Group and Paleocene sediments of the Huanca Formation. The basement is composed of Proterozoic high-grade metamorphic rocks (the Charcani gneiss, e.g., Wilson, 1986; Ramos, 2008 and references therein).

Since Middle Miocene times, the Arequipa basin has been filled by a succession of ignimbrites of different ages (Paquereau-Lebti, 2006, 2008; Thouret et al. 2001, 2016) (see section 5.1). These ignimbrites are variably eroded and overlain by more recent volcanoclastic, alluvial and glacial wash-out deposits derived from the overlying younger volcanic edifices of El Misti volcano and the Chachani cluster. The close association in time and space between the Chachani cluster and the youngest Arequipa Airport Ignimbrite (AAI) as well as the depositional features (Fig. 3B) suggests that the C-LVC has probably been built over a caldera from which the AAI was erupted (Garcia et al., 1997; Paquereau-Lebti et al., 2006, 2008). Paquereau-Lebti et al. (2008) measured anisotropy of magnetic susceptibility (AMS) and componentry that confirm that the source of the AAI sheet was located underneath the C-LVC. The 13 km long, N-S oriented, arcuate scarp 9 km to east of Chachani has been interpreted from satellite images as the possible rim of the proposed "Chachani caldera" (Fig. 3B; Garcia et al., 1997). The AMS measurements, however, did not provide evidence for the source location of the Río Chili and La Joya ignimbrites, so RC and LJ sources are poorly constrained but presumed to be somewhere on the Altiplano beyond El Misti volcano and near the Sumbay valley northeast of the C-LVC (Paquereau-Lebti et al., 2008).

3.2. Transpressional tectonic regime in oblique convergent margin

The active continental margin has long been described as the result of archetypal Andean subduction (Thorpe, 1982; Wilson, 1986; Stern, 2004), which, in southern Peru, has developed by oblique convergence (Ramos, 2010; Armijo et al., 2015). The present-day range of arc volcanoes, located 220-250 km east of the Peru-Chile Trench and above a 30° dipping slab, formed upon the Western Cordillera (Figs. 2 and 3A). The maximum compressive stress (σ_1= N80°E) is accommodated by N130°E and N160°E strike-slip faults at least since Cenozoïc times (Mering et al., 1996; Sempere and Jacay, 2006, Sempere et al., 2014). The transpressional tectonic regime affects the SW flank of the Western Cordillera at the northern edge of the Arequipa basin, as sketched in Figure 3C. The WNW-ESE–trending Arequipa depression has been interpreted as a pull-apart basin at the intersection of ~N130ºE strike-slip and normal faults, and N10º and N40º faults (Mering et al., 1996; Thouret et al., 2001, Benavente et al., 2017). The active, N130°E strike-slip faults parallel the Western Cordillera, e.g., the Ayo-Lluta-Arequipa and Río Chili faults that cut the SE flank of Chachani and El Misti stratocone, and the Aguada Blanca fault on the East side of C-LVC. The Western Cordillera parallels active, normal and strike-slip N130° faults, while the oblique N80°E convergence is accommodated by en-echelon N160°E faults (Fig. 3C).

Individual arc volcanoes like El Misti, Ubinas, and Chachani straddle the faulted flank of the Western Cordillera on the northern edge of the pull-apart basin of Arequipa (Gonzales et al., 2014). As a result of the pull-apart basin in transpressional setting, N80º-trending, active normal faults cut the flank of the Western Cordillera in a series of staircase looking south (Figs. 3A and 5). This asymmetry likely has implications on edifice growth, alignment and migration of vents, and potential edifice instability due to the steeply SW-ward dipping base (Fig. 3C).

The C-LVC has been built up in a complex structural setting (Figs. 3A-C, 5). A group of edifices in the north and east are aligned along reverse and strike-slip N160°E faults (Figs. 3A and 4); whereas, in the central part of the C-LVC, a group of edifices has grown along N80°E-trending structures that cut out staircases looking south in the folded, Mesozoic sedimentary rocks of the Western Cordillera (Figs. 3A and 4**)**. These staircase structures of the south WC flank looking south appear on 2D diagrams (Fig. 6) that help reconstruct the approximate pre-Chachani palaeo-topography. On the south flank of the C-LVC, the Airport-Potrero dome-coulee complex and several small vents are aligned along N10°E and N40°E open eruptive fissures that fed extensive aa and block-lava fields to the south and SW (Fig. 3A).

253 ## 4. METHODS

254 ### 4.1. Geological mapping and sample collection

255 The geological map (Fig. 4) was compiled from preliminary fieldwork carried out by Suaña
256 (2011) and our additional fieldwork, coupled with interpretation of SPOT5 (2.5 m pixel) and
257 Google Earth satellite images. Satellite imagery and SRTM-based DEM-shaded reliefs enabled
258 us to define and delineate the position and elevation of contacts between the C-LVC and its
259 inclined base around the volcano and inside the Río Chili canyon to the east. Individual volcanic
260 edifices of the C-LVC were distinguished based on observed morphological, erosional, and
261 angular discordances. The location of visible craters and vents and uniform surface
262 morphologies and satellite image colors further allowed us to delineate twelve individual
263 volcanic edifices comprising the C-LVC. In several cases, it was also possible to identify, lower,
264 middle and upper stratigraphic units within a volcanic edifice based on observed overlap, inset
265 landform relations, and stratigraphic unconformities that allowed us to separate different stages
266 of lava flow eruptions. Edifice boundaries and stratigraphic units were embedded in a GIS-
267 based 1:25,000 scale topographic map. Sub-units have been labeled using the first three letters
268 of the edifice name, followed by a number pointing to its stratigraphic position (e.g., Noc1 is
269 the basal unit of the Nocarane edifice; Fig. 4).

270 Based on our new geologic map and the 30-m SRTM DEM data, we calculated the total volume
271 of the C-LVC with three different tools and techniques. We used (1) Surfer® and (2) ArcMap®
272 software to perform a difference between the DEM elevation (actual topography) and the 3-D
273 reference basal surface beneath the C-LVC (topography without the C-LVC; more details in
274 section 8.1). Additionally, we computed the volume using (3) MORVOLC algorithm (Grosse
275 et al., 2012).

276 During fieldwork, representative samples of lavas were collected for petrographic and
277 geochemical analysis. Samples for the radiometric dating were taken specifically from the base
278 and top units of the volcanic edifices in order to best constrain the period of activity of each
279 edifice.

280 ### 4.2. Analytical methods

281 #### *4.2.1. Mineralogy and geochemistry*

282 Thin sections of fifty-two fresh samples allowed us to describe most of edifice lavas of the C-
283 LVC. Given that the mineral assemblage is rather homogeneous, the number of samples is
284 thought to be representative. Major element composition for main mineral phases of fourteen

representative samples were analyzed at the Laboratoire Magmas et Volcans (LMV), Université Clermont Auvergne (Clermont-Ferrand, France) using a Cameca SX-100 electron microprobe (See ESD Table 2). The most representative textures were analyzed to recognize composition changes during crystal growth and infer petrogenetic processes. For geochemical analyses, sixty-eight samples were crushed and milled in an agate mortar. For major element analysis, powdered samples were mixed with $LiBO_2$, placed in a graphite crucible, and melted in an induction oven at 1050°C for 4.5 min, resulting in a homogeneous glass bead. The glass was then dissolved in a solution of deionized water and nitric acid (HNO_3) and finally diluted by a factor of 2000. The final solutions were analyzed by ICP-AES (Jobin-Yvon ULTIMA C) at LMV. Trace element analyses have been carried out by ICP-MS at the Centre de Recherche Pétrographiques et Géochimiques in Nancy, France. These new data were combined with previously analysed rock samples from Chachani reported in Mamani et al. (2010).

4.2.2. Dating techniques

$^{40}Ar/^{39}Ar$ geochronology

Alkali feldspars (average K/Ca= ~ 1) were isolated from pyroclastic rocks and groundmass / glass separates were prepared via magnetic and density separation using methylene iodide. All purified separates were weighed and then irradiated at the Oregon State University TRIGA reactor in the Cadmium-Lined In-Core Irradiation Tube (CLICIT). $^{40}Ar/^{39}Ar$ incremental heating experiments were undertaken on groundmass/glass separates following Jicha et al. (2012). Single crystal fusions were performed on the feldspar separates following the methods of Meyers et al. (2012). Argon isotope analyses were done using a MAP 215–50, and the data was reduced using ArArCalc software version 2.5 (http://earthref.org/ ArArCALC/). All age data presented here are calculated relative to 28.201 Ma for FCs (Kuiper et al., 2008), the decay constants used are those of Min et al. (2000), and the age uncertainties reported in Table 2 reflect only analytical contributions at the 2σ level.

La-ICP-MS U-Pb geochronology

U-Th-Pb isotopic data on separated zircons were obtained by laser ablation inductively coupled plasma spectrometry (LA-ICP-MS) at LMV. The analyses involved the ablation of minerals with a Resonetics M-50 Excimer laser system operating at a wavelength of 193 nm coupled to a Thermo Element XR Sector Field ICP-MS. Spot diameters of 33-44 were associated to repetition rates of 3 Hz and fluency of 3 J/cm^2. The analytical method for isotope dating, U-Pb fractionation and mass bias corrections and quality control is basically similar to that reported

in Hurai et al. (2010), Paquette et al. (2014), and Mullen et al. (2018). Data reduction was carried out with the software package GLITTER® from Macquarie Research Ltd (van Achterbergh et al., 2001). ^{230}Th disequilibrium was corrected according to Schärer (1984). Concordia ages and diagrams were generated using Isoplot/Ex v. 2.49 software package by Ludwig (2001). The zircon analytical results were projected on ^{207}Pb/^{206}Pb versus ^{238}U/^{206}Pb diagrams (Tera and Wasserburg, 1972).

^{40}Ar/^{39}Ar ages indicate cooling in groundmass (i.e., eruption ages) whereas U/Pb indicate crystallization age of the analyzed zircon crystals. Considering their uncertainties, there are no age discrepancies between chronology and stratigraphy for main groups of edifices. Thus, we used these dates to constrain the temporal evolution by distinguishing chrono-stratigraphic intervals of edifices into a long-lived system such as the C-LVC. However, our age, volume and eruption-rate estimates have high uncertainties when it comes to individual edifices. Similar dating methods were used to correlate the stratigraphy of Neogene and Quaternary ignimbrites in southern Peru (Thouret et al., 2016). Table 2 indicates the two different groups of ^{40}Ar/^{39}Ar data with (^{1}) exponent and U/Pb data with (^{2}) exponent. ESD Table 3 displays analytical data for ^{40}Ar/^{39}Ar ages.

5. ERUPTIVE CHRONOLOGY

5.1. Pre-Chachani: ignimbrites and lava flows

The bedrock of the C-LVC consists of a series of rhyolitic ignimbrite sheets described by Paquereau-Lebti et al. (2006, 2008) and volcaniclastic deposits that crop out in the Arequipa basin and the Río Chili canyon (Figs. 4 and 5).

1. The Río Chili ignimbrite (‘Chuquibamba’ *c.* 13.12–13.19 Ma; Thouret et al., 2001, 2016) exposed at the base of the Río Chili canyon overlying older strata displays a massive, up to 140 m thick cooling unit, with non-welded to partially welded crystal-rich deposit.

2. The La Joya ignimbrite ‘LJI’ (*c.* 4.86-4.89 Ma; Paquereau-Lebti et al., 2006) filled the Arequipa basin and mantled part of the Arequipa Batholith to the SE of the basin.

3. The Arequipa Airport Ignimbrite ‘AAI’ (20-25 km^3) consists of two units with weighted mean ages of 1.66 ± 0.07 Ma for the lower white unit and 1.62 ± 0.04 Ma for the upper pink flow unit (Paquereau-Lebti et al., 2006, 2008). The source of these ignimbrites is not exposed but is thought to be buried below the C-LVC. This is indicated by anisotropy directions of

magnetic susceptibility measurements and the size of lithic fragments contained in the upper AAI pink unit, which increases northward towards Chachani (Paquereau-Lebti et al., 2008). The upper AAI unit is overlain by a 1.41 ± 0.25 Ma old pyroclastic density current (PDC) deposits close to Nevado Chachani (e.g., Cerro Colorado, airport area; Paquereau-Lebti, 2006).

4. A series of black, vesiculated and plagioclase-rich lava flows crops out in the La Paccha riverbed at the west margin below younger lavas from Nocarane stratovolcano (Fig. 4). These lavas are overlain by the Yura tuffs (YT) and therefore these lavas are considered to form the local bedrock of Quaternary age.

5. The Yura Tuffs 'YT' (Jenks, 1948) are a series of non-welded ignimbrite deposits with intercalated layers of reworked volcaniclastic deposits. The YT (1.5 km^3) have been $^{40}Ar/^{39}Ar$ dated at 1.28 ± 0.05 Ma (on plagioclase) and 1.03 ± 0.09 Ma (on biotite: Paquereau-Lebti et al., 2006). YT deposits are restricted to the north and west sides of the C-LVC, filling a north-south elongated depression between the sedimentary 'Yura' Group of Jurassic age (Wilson and García, 1962) and the Pre-Chachani lava bedrock (Fig. 3A). The source of the YT lies below the lava flows of the Baquetane volcano north of the C-LVC.

6. Deposits of the Capillune Formation (Guevara, 1969) overlap the La Joya Ignimbrite to the east of C-LVC. Based on the stratigraphic position below Pre-Chachani lava flows and geochemical correlations (Paquereau-Lebti et al., 2008) with the Yura tuffs, the Capillune Fm. may be of similar age, i.e., between 1.63 Ma and 1.28 Ma. A 20-km-wide depression suggests the existence of an older caldera of Plio-Quaternary age (Garcia et al., 1997), now filled by 10 to 30 m-thick sequence of non-welded pyroclastic flow and tephra-fall deposits intercalated with lacustrine deposits of the early Pleistocene Capillune Fm to the east of C-LVC and north of El Misti volcano (Fig. 3A), and ignimbrites of the *c.* 4.86-4.89 Ma LJI (Paquereau-Lebti et al., 2006).

5. 2. Volcanic evolution of C-LVC

We distinguish two groups of 'Old Edifice' and 'Young Edifice' and investigate to which extent the C-LVC and earlier ignimbrite magmas in the same area may be related. Based on 1:25,000 scale mapping, identification of structural growth patterns and stratigraphic relationships, together with twenty $^{40}Ar/^{39}Ar$ and U/Pb ages (Figs. 4 to 6, Table 2), we reconstruct the eruptive chronology of the C-LVC, which is characterized by recurrent activity and short periods of quiescence.

5.2.1 Old Edifice group lavas (*c.* 1280–640 ka)

The early Pleistocene Old Edifice group was built between *c.*1280 and 640 ka and form the eastern and northern parts of the C-LVC (Table 2). The largest individual volcanic structures (Nocarane, Estribo and Chingana) and the smaller El Colorado dome coulees follow a N150°-N160° arcuate trend.

The C-LVC basal lava flow unit

The initial activity of C-LVC produced andesitic lava flows that cover an area of 25 km^2 and represents a volume of 1.33 - 3.62 km^3 (Fig. 4, Table 2). The lowest unit was directly emplaced onto the YT on the NW side of the C-LVC, but middle and upper units are intertwined with the YT. The second unit of lava flows on the SW flank of the C-LVC overlies a thin unit of alluvium deposits just above the upper unit of the AAI. The age of these basal flows therefore is between *c.*1280 ka (Yura Tuff age) and *c.* 1010 ka (i.e., the onset of the overlying Chingana edifice).

Chingana stratovolcano

Located on the NE side of the C-LVC, Chingana (44 km^2, 32.10 - 47.40 km^3) is the oldest exposed stratovolcano of the cluster. Lavas exposed at its base (U/Pb age of 1012 ± 53 ka, Table 2) reached a distance of 7 km from the vent. The flanks were partly buried by the younger Nocarane and El Angel edifices. The middle unit is made up of andesite $^{40}Ar/^{39}Ar$ dated at 916 ± 41 ka (Table 2). The upper unit of Chingana consists of basaltic andesite lava flows that are the least silicic (53.68 wt.% SiO_2) of all observed C-LVC lavas.

Nocarane stratovolcano

The 121 km^2, 65.53 - 125.93 km^3 and 5760 m-high Nocarane stratovolcano, dated between *c.* 916 and 641 ka (Table 2), consists of a thick pile of andesite lava flows topped by lava domes. Three overlapping units include: (1) the lower unit on the NW part of the edifice that consists of scoria deposits (Noc1) and dark lava flows with restricted tephra-fall deposits (Noc2-Noc4). (2) Block-lava flows and domes were emplaced on the top and towards the NNW flank. An andesitic dome, now glaciated, was emplaced at high elevation (5400 m) just north of the summit (Noc10) and yielded a U/Pb age of 866 ± 71 ka (Table 2). (3) The morphologically most recent flow forms the summit plateau at 5748 m asl (undated). A flat dome in the middle of the 500 m-wide cirques at the summit open to the west is also still partly preserved and could represent a glacially eroded crater fill. On the lower flanks, a succession of dark gray lava flows extends to NE as far as ~9.3 km (Noc11–Noc14). One of these andesitic lavas (Noc15) on the lower western flank was $^{40}Ar/^{39}Ar$ dated at 754 ± 10 ka, which represents the youngest dated unit of Nocarane. Based on our dating and the similar morphology of all flows on the lower

412 flanks of Nocarane, the period of activity of this volcano was rather short and restricted between
413 870 and 750 ka. This age range largely overlaps with dates from Estribo and Colorado centers
414 (see below and Table 2) and thus marks a time of focused andesite eruptions at C-LVC.

415 ***Estribo stratovolcano***

416 This sizeable stratovolcano (120 km^2 and 59.35 - 63.03 km^3) is located on the SE edge of C-
417 LVC (Fig. 4). Since Río Chili has cut a canyon into the base of the C-LVC and the bedrock at
418 the SE margin of Estribo, it exposes older Early Quaternary ignimbrites, a 200-300 m thick
419 volcaniclastic succession of unknown origin, and the earliest pyroclastic deposits and lava flows
420 sourced from the Estribo center. Later, this canyon was partly filled by middle Pleistocene
421 debris-avalanche deposits from Estribo (Bernard et al., 2017). The base of Estribo exhibits
422 volcanoclastic sediments overlain by hydroclastic deposits (Fig. 4, HR in Fig. 5A) that contain
423 decimeter-sized glassy breadcrust bombs and associated breccia and lapilli tuffs with
424 intercalated, coarse, normally graded pumice-fall layers. These deposits were partly
425 palagonized after wet deposition and are probably related to sub-glacial eruptive processes.
426 These deposits are conformably overlain by subaerial block-lava flows of the middle Estribo
427 unit.

428 The volcaniclastic succession below the Estribo deposits overlies the 1.62 Ma upper pink-unit
429 of the AAI as well as the 1.40 Ma PDC and tephra-fall deposits that are exposed west of
430 Arequipa (Thouret et al., 2001; Paquereau-Lebti et al., 2006). The pyroclastic sequence includes
431 intercalated tephra and PDC deposits in channel fills (Wegner and Ruprecht, 2003) and thins
432 out towards the SE below the oldest Estribo and El Misti lava flows. Distally to the SW, this
433 volcaniclastic succession encompasses lahar deposits intercalated with pumice-fall deposits and
434 thins out towards the basin of Arequipa. Debris-avalanche and lahar deposits suggest that
435 erosion and collapse affected the earliest C-LVC edifices towards the Arequipa depression.
436 This volcaniclastic fan therefore suggests a depositional period of intertwined eruptive activity
437 possibly from a "palaeo-Estribo" volcano and other Old Edifice group located below the
438 younger Chachani edifices. Their facies indicate extensive interactions between volcanic and
439 glacial activity and their age falls between the older dated ignimbrite eruptions (1.40 Ma) and
440 the base of Estribo (*c.* 746-871 ka). As such, these deposits represent the earliest post-caldera
441 products between the formation of the underlying older ignimbrites and the initiation of eruptive
442 activity of the present C-LVC edifices (Fig. 5).

443 The earliest lava flows of the Old Edifice group from the basal unit of Estribo consist of
444 andesitic and dacitic lavas (Est1–Est5) that flowed down ~10 km to the south of Estribo's
445 summit. A pronounced angular unconformity located at about 4800 m distinguishes the lower
446 from middle units. The middle unit consists of andesite lava flows and scoria-fall and flow
447 deposits (Est6). One flow of the upper units of this eruptive center (Est8) is 808 ± 63 ka
448 ($^{40}Ar/^{39}Ar$) old, while the most recent lava flow (Est10) is 694 ± 75 ka ($^{40}Ar/^{39}Ar$). Andesitic
449 lava flows that extend ~10.4 km to the NE of the vent partly covers deposits of the Chingana
450 stratovolcano. These Estribo flows overlap in age with a lava flow exposed at the base of El
451 Misti on its lower W flank and across on the northern side of Río Chili canyon, which was dated
452 at 833 ± 6 ka (Thouret et al., 2001). This flow had previously been considered to be a precursor
453 to El Misti volcano (≤ 112 ka). However, with the new ages of C-LVC and the observed
454 stratigraphic relations, this lava flow is more likely part of the Estribo edifice.

455 ***El Colorado dome coulees***

456 El Colorado (12.3 km^2 and 4.13-6.16 km^3) is the northernmost composite dome-coulee complex
457 of the C-LVC. It has been built by extrusive pulses of two superimposed porphyritic andesite
458 domes coulees $^{40}Ar/^{39}Ar$ dated at 642 ± 88 ka on the WNW lower flank of Nocarane
459 stratovolcano. At the top of the highest dome coulee, a breached vent, now occupied by a dome,
460 was the vent for a lava flow that propagated 2.2 km to the northeast and overlapped the two
461 domes coulee units. The subdued but preserved, ropy lava flow surface is consistent with the
462 relatively young age compared to the other the Nocarane flows and thus represents the most
463 recent event of the Old Edifice lavas of the C-LVC.

464 **5.2.2 Young Edifice group lavas (*c.* 460–56 ka)** A series of younger, Middle to Late
465 Pleistocene edifices is aligned south and SW of the Old Edifice group. The Young Edifice lavas
466 have built a 12.5-km long edifice that now forms a glaciated WSW-ENE ridge (N80°E) across
467 the south-sloping pre-Chachani basement (Figs. 3, 4). Extrusive activity of the Young Edifice
468 group has produced abundant cumulo-domes, dome coulees and block-lava flow fields, which
469 are morphologically better preserved compared to the Old Edifice group. Their vents are aligned
470 along the N80°E ridge formed by these edifices, while the Cabrería dome vents (~56 ka, Table
471 2) are also aligned N80°E on the southern flank of Estribo stratovolcano.

472 ***El Angel stratovolcano***

473 El Angel is a small stratovolcano (~13 km^2, 4.86 - 5.56 km^3) made up of a succession of four
474 andesite lava flows (Ang1−Ang4). Two craters are still visible on the top of the edifice which

has been eroded to the west flank over which the younger Chachani summit lavas were emplaced. To the E, lavas have covered the youngest lavas of Chingana and Estribo stratovolcanoes. Zircons from a lava unit covered by Nevado Chachani stratovolcano were U/Pb dated at 463 ± 34 ka. As El Angel is morphologically better preserved and shows at least ~200 kyr difference with surrounding edifices (Chingana and Estribo), which is not observed in both groups' eruptive hiatus, this stratocone may be the earliest of the aligned Young Edifice group of the C-LVC.

Airport-Potrero dome cluster

Dome-coulees and stubby lava flows form a prominent, complex landform between 5 and 15 km SW of the summit of Chachani. This dome complex shows both large areal extent (*c.* 68 km^2) and volume (between 11.22 and 12.53 km^3). Single, up to 100 m thick and stubby block-lava flows issued from a cluster of dome-coulees. The lower and middle units of the Airport-Potrero dome cluster dated by $^{40}Ar/^{39}Ar$ at 397 ± 40 ka (PD1) and 369 ± 62 ka (PD3), respectively, consist of porphyritic lavas with composition straddling the boundary between the andesite and dacite fields (62–64 wt.% SiO_2, Fig. 8). The middle unit (PD 4-7) also consists of dacite, whereas the upper unit lavas (PD 8-10), $^{40}Ar/^{39}Ar$ dated at 292 ± 5 ka, shows a silicic andesite composition. The uppermost unit (undated) shows a 1.8 km-sized ring-shape subsidence in the central part affecting the most recent dome coulees. A series of craters are aligned along N10º-40ºE and N130ºE eruptive fissures (Fig. 3A) that may have controlled the growth of the dome and stubby lava-flow complex. Available ages indicate a *c.*100 kyr-long effusive activity for the Airport-Potrero dome cluster (Fig. 4).

La Horqueta cumulo-dome

La Horqueta (40 km^2, 3.24 – 6.46 km^3) is a pile of superimposed domes with steep, overlapping, stubby block-lava flows located in the central part of the younger edifice. Its lava flows extend as far as 13 km southeast towards El Rodado and to the northwest it is covered by younger flows of Nevado Chachani summit. The "lower unit" consists of andesite block-lava flows (Hor1–Hor2). The middle unit, dated by U/Pb at 345 ± 26 ka, consists of andesite lava flows (Hor3 and Hor4) that reached a ~6.3 km distance from the vent to the northwest. A pile of andesite lava flows is found on the southeast side of the edifice as far as ~7 km from the summit. One flow of the upper unit was U/Pb dated at 332 ± 29 ka.

El Rodado stratocone

Flows from the El Rodado (50 km^2, 6.26 – 9.17 km^3) edifice overly the La Horqueta cumulo-dome on its western flank. The lower unit is formed by andesite lava flows (Rod1 and Rod2). Distally they cover older weathered volcanoclastic deposits that mantle the AAI on the upper slopes of the basin. The middle unit consists of porphyritic andesite lava flows (Rod3–Rod5), one of which was U-Pb dated at 239 ± 25 ka. The upper unit of El Rodado, which was emplaced on the collapsed side of the middle unit, consists of andesite lava flows (Rod6 and Rod7). The eruptive activity of the upper unit followed the Late Pleistocene collapse of the southern flank of the middle unit, which left a 1.2 km-wide amphitheater open to the south.

The Uyupampa compound lava-flow field

A thick (~100 m) and stubby, compound aa and blocky lava-flow field (Uyu1 to Uyu3) of 16 km^2 and 2.36 – 2.72 km^3 form the westernmost edge of the Chachani cluster. This andesitic, compound field of blocky lava flows cover the lava flows of the El Rodado stratocone. The second lava-flow field unit has an $^{40}Ar/^{39}Ar$ age of 232 ± 36 ka. While the El Rodado edifice is morphologically older than the Uyupampa flows, their ages overlap within error. This indicates that their activity was closely related in time.

The Nevado Chachani stratocone

Nevado Chachani summit edifice (45 km^2, 30.34–33.20 km^3) forms the most recent and highest stratovolcano of the C-LVC, towering at 6057 m asl. It consists of three units that were emplaced in the central part of the Young Edifice group. The lower unit is located on the eastern side of the summit complex, overlying El Angel stratovolcano (Cha1−Cha5). Block-lava flows from the middle unit (Cha6 –Cha8) that cover the deposits of the La Horqueta cumulo-dome were dated by U/Pb at 222 ± 24 ka and 202 ± 32 ka. A small, flattish andesite lava dome named La Torta (Fig. 3A), probably emplaced under subglacial conditions as it displays glassy, prismatic lava flow edges, is considered as part of this unit. The upper unit, emplaced over the collapsed side of the lower unit, consists of andesite and dacite lava flows that have yielded young $^{40}Ar/^{39}Ar$ ages of 131 ± 4 ka and 130 ± 38 ka. At the apex of the lava flows, which were weathered beneath the former summit Ice cap, we observe four youthful craters.

Cabrería dome-coulees

These units consist of lava domes (Cab) and aprons of thick block-and-ash flow deposits, one of these deposits being dated by $^{40}Ar/^{39}Ar$ at 56 ± 31 ka. The widespread (> 21 km^2, 4.13 – 4.91 km^3) pyroclastic apron up to 9 km down towards the Arequipa airport and the town of Cayma

represents one of the most recent pyroclastic deposits from dome collapse events on the south flank of Nevado Chachani.

El Volcancillo dome

A small (~1.2 km^2, 0.33- 0.39 km^3) dacite lava-dome and a small lava flow (Vol) were emplaced in a large glacial scar open to the west near the summit of Chingana stratovolcano. Its location and lack of glacial erosion despite its elevation (~5200 masl) suggest that this is the most recent (Late-Glacial times?) center of the C-LVC. Various attempts at $^{40}Ar/^{39}Ar$-dating this lava dome have, however, failed due to its young age and excess argon. However, based on morphological observation, we propose to include the El Volcancillo dome into the Young Edifice group.

5.2.3 Evidence for a stratigraphic gap

During fieldwork, mapping, and sampling, we have not found other C-LVC deposit overlying the dated *c.* 641 ka unit of El Colorado dome (the youngest of the Old Edifice group). In addition, one of the lowermost units of El Angel edifice dated at *c.* 463 ka (i.e., the oldest of the Young Edifice group) directly overlies the Chingana edifice. Thus, a distinct magmatic gap from *c.* 641 to 463 ka (Fig. 4) is documented between the Old Edifice group (*c.*1280 and 640 ka) and the Young Edifice group (*c.* 460 – *c.* 56 ka).

5.3 Late Pleistocene pyroclastic sequences of C-LVC

Late Pleistocene pyroclastic deposits are almost absent on the upper flanks of C-LVC and were probably covered by subsequent lavas and/or removed by glacier ice and meltwater above 3800 m asl. However, tephra-fall and PDC deposits, found on the lower flanks of the Old Edifice group, for example on the north flank of Nocarane (beneath El Colorado dome), on the south flank of the Estribo and lower east flank of Chingana edifices, are related to explosive activity. Scoria flows including glassy breadcrust bombs indicating phreatomagmatic or subglacial activity crop out on the western flank of the Nocarane edifice. The source is probably a scoria cone located at 5.5 km distance at 4700 m (16°07'19.95S, 71°34'05.21W).

More extensive and thicker pumice-rich lapilli fall layers are intercalated in El Misti PDC and tephra successions on the SW and south flanks of Nevado Chachani, as well as in outcrops towards the city of Arequipa (Independencia and Quebrada Pastores, Fig. 4). The 4 to 7 m-thick pumice-fall sequence with distinct greenish color, scoriaceous texture, and mafic andesite composition crops out between the 70-ka lava flow observed in the Quebrada Pastores valley and the *c.* 46 ka 'Misti 2.2' PDC sequence (Thouret et al., 2001).

In the Young Edifice group, block-and-ash flow deposits are related to the Airport-Potrero and the Cabreria domes (56 ± 31 ka, Table 2) on the lower south flank of the C-LVC.

Major Holocene activity at the Nevado Chachani volcanic cluster cannot be ruled out, although no tephra depositor lava flows of that age have been identified so far. However, four breached and unglaciated craters are preserved on the stratocone summit, and two vents adorn the eroded summit ridge of the El Angel composite cone. These small summit craters could well be related only to minor phreatic eruptions. Given the relatively young ages and extended periods of activity and quiescence in the geological past, the southern Young Edifice group, in particular the Nevado Chachani and El Angel stratocones should be considered presently dormant and eruptions in the geological future should be expected.

6. SUMMARY OF PETROGRAPHY AND MINERALOGY

Modal analyses of the sample dataset are given in Table 5. Modal analyses of the analysed samples are given in Table 5. We refer the readers to ESD Petrography and Mineralogy, Table 2 and ESD Figures 1-5 for further petrographic and mineralogical descriptions of the C-LVC lava flows. Lavas of the Old Edifice group contain 6-38 vol.% phenocrysts (>500 µm) and micro-phenocrysts (100-500 µm), and 62-94 vol.% groundmass (glass and microlites). The most common phenocrysts and micro-phenocrysts include plagioclase (5-31 vol.%), amphibole (1-8 vol.%), and ortho- and clinopyroxene (<7 vol.%), with olivine and biotite as accessory minerals (Fig. 7), and rhyolitic glass (68-77 wt.% SiO_2).

The Young Edifice samples contain 13-45 vol.% phenocrysts and micro-phenocrysts, and 55-87 vol.% groundmass. The dominant phenocrysts and micro-phenocrysts are plagioclase (11-35 vol.%), amphibole (1-10 vol.%), ortho- and clinopyroxene (<5 vol.%), biotite is accessory mineral, while olivine micro-phenocrysts are present only in lavas from La Torta dome (Fig. 7). The groundmass of andesites and dacites is comprised of plagioclase, amphibole, pyroxene, and rhyolitic glass (73-78 wt.% SiO_2). As a whole, the mineral assemblage and the mineral chemistry remain the similar during the entire C-LVC evolution (see ESD Table 2). However, we observed a few differences; for instance, the fact that amphibole and biotite tend to be more abundant in the felsic lavas, whereas olivine only appears in one basaltic andesite lava. In addition, a few minerals (i.e., plagioclase and amphibole) display different textural types that include euhedral, non-altered phenocrysts together with phenocrysts, showing frequent disequilibrium textures such as spongy cellular (sieve) textures with cores, and concentric

growth zones and/or dissolution zones as well as late overgrowth rims in plagioclase. We also note different types of amphibole breakdown textures, the fine-grained opaque rims from dehydration that form during fast decompression and eruption and the coarse-grained breakdown zones indicative of slower ascent (Rutherford and Hill, 1993). Both types of disequilibrium textures are more frequent in the Young Edifice compared to the Old Edifice group.

7. TEMPORAL WHOLE-ROCK COMPOSITIONAL VARIATIONS

7.1. Evolution of major elements through the C-LVC lifetime

Chemical data of bulk rock composition indicate three different patterns through time (Figs. 8 and 9**,** ESD Table 3**)**: (1) the oldest Pre-Chachani lava units (>1.28 Ma) which crop out at the Quebrada La Paccha show homogeneous lava compositions (mean = 60.12 wt.% SiO_2, SD= 0.10, N= 5). (2) The Old Edifice lavas (~1.00–0.64 Ma) display a wide range in silica content (mean= 60.88 wt.% SiO_2, SD= 2.88, N= 62), whereas (3) the Young Edifice group lavas (0.46–0.05 Ma) again show a narrow compositional range (mean= 61.54 wt.% SiO_2, SD= 1.44, N= 39). In the following descriptions, we will focus on both C-LVC lava groups, while we will not describe the Pre-Chachani lavas..

7.1.1. Compositional variations throughout the Old Edifice group

Whole rock compositions (Figs. 8, 9) within the Old Edifice group change from andesite in the "Upper Base Chachani" (~1.1 Ma) to basaltic andesite in the Upper Chingana stratovolcano (~0.91 Ma). Composition from the Estribo stratovolcano changes along a narrow but reverse trend with a swift variation from dacite (Lower Estribo unit) to andesite (Middle Estribo unit). The third edifice (Upper Estribo ~0.81 Ma) follows a common differentiation trend from andesite (59 wt.% SiO_2) to dacite (64 wt.% SiO_2), but the most recent Estribo lavas (~0.69 Ma) exhibit a decrease in SiO_2 content (~62 wt.%). Lavas from Nocarane starts with dacite compositions (66 wt.% SiO_2), and then show a trend from dacite to basaltic andesite and again to dacite in the same unit (Lower Nocarane ~0.75 Ma). From Middle to Upper Nocarane, the composition changes reversely to ~60 wt.% as does El Colorado dome (~58 wt.%).

7.1.2. Compositional variations throughout the Young Edifice group

The Young Edifice group display a smaller range in compositions (59–64 wt.% SiO_2; Figs. 8, 9) compared to the Old Edifice lavas. Lavas of El Angel composite volcano, that represent the

older flows of the Young Edifice group, display andesitic compositions (62-63 wt.% SiO_2). In contrast, the peripheral Airport-Potrero Domes shows a wider compositional range from andesites to dacites (59-64 wt.% SiO_2). Then, La Horqueta lava domes and El Rodado cone show compositions limited to a relatively narrow andesite range (60–63 wt.% SiO_2). The central Chachani composite volcano starts with slightly evolved dacites, but lavas change to andesites with a decrease in SiO_2. Finally, the most recent eruptive activity of the C-LVC from the Cabrería and Volcancillo domes again produced slightly more evolved lavas (62–64 wt.% SiO_2).

7.2. Trace element patterns through C-LVC lifetime

A few trace elements (e.g., Ni, Cr, V, Sc, Sr and Eu; ESD Fig. 7) are negatively correlated with SiO_2 contents, although scattering is observed in Ni, Sr and Cr. In lavas of the entire C-LVC, chromium and nickel contents are low (< 90 and < 60 ppm, respectively). Only the less differentiated basaltic andesite samples exceed these values in the Chingana and Nocarane edifices. Large-ion-lithophile elements (LILE; e.g., Cs, Rb, K, Ba) are positively correlated with SiO_2, except Sr, which displays a negative correlation, and Eu content that remains constant throughout differentiation (not shown). Th and U display a moderate positive correlation with SiO_2, whereas high field strength elements (HFSE, e.g,, Nb, Ta, Zr, Hf) and light rare earth elements (LREE, e.g., La, Ce, Nd) exhibit a slightly positive correlation with SiO_2 increase. Middle and high rare earth elements (MREE and HREE; Sm and Y) show no variations with increase in silica contents.

Primordial Mantle-normalized spider diagrams of the C-LVC lavas (Fig. 10) exhibit strong enrichment in LILE (Rb, Ba, K, Sr) compared to HFSE (Nb, Ta), a typical feature for subduction-zone magmas, especially those of the CVZ (e.g., Wilson, 1986). Old Edifice lavas display stronger enrichment and wider ranges in Rb, Ba, Th and U, slight enrichment in Sr and Y, and stronger depletion in Cs, Nb and Ta (Fig. 10). Young Edifice of the C-LVC exhibit a unique pattern: all of them are strongly depleted in Nb and Ta, but slightly enriched in La and Sr. The trace element distribution patterns are more uniform in the Young Edifice lavas than those of the Old Edifice group.

7.3. Chemical correlation between the C-LVC and the AA Ignimbrite

The C-LVC has buried the source (large nested vents or a single caldera) of the AAI (Paquereau-Lebti et al., 2006, 2008) within only several 100 ka. A genetic link and an evolution

662 in a common magmatic system should therefore be considered by testing their potential
663 geochemical relations.

664 Major element oxides in Harker diagrams and plot of incompatible elements (Cs, Rb, K and
665 Ba) against silica content suggest that C-LVC, AAI and LJI magmas form a single
666 differentiation trend (Fig. 11). On the other hand, LJI is enriched in Rb and Cs (not shown) but
667 is depleted in Ba compared to AAI. Ratios of K, Rb and less incompatible elements like Dy,
668 Ta, Yb, Nb indicate that the C-LVC and AAI follow a similar trend; in contrast, LJI shows
669 dispersed values (Fig. 11). For instance, Rb/Sr *vs*. SiO_2 diagram shows that C-LVC lavas and
670 AAI fall in the same differentiation pattern, whereas LJI display higher Rb/Sr values for similar
671 silica contents. Incompatible-element ratios such as Ba *vs* Th and B/Th *vs*. Dy/Yb (Fig. 11)
672 exhibit overlapping fields with higher values in Ba/Th in C-LVC and AAI samples compared
673 with lower Ba/Th ratios in LJI samples.

674 The gap in silica content between C-LVC lavas and ignimbrite sheets (from 66 to 75 wt.% SiO_2)
675 indicates that the more silicic magmas represented by the ignimbrites are significantly more
676 evolved and are affected by the dominant fractional crystallization of plagioclase and K-
677 feldspar. We document this process through the increasing Rb/Sr and decreasing Ba for
678 comparable SiO_2 and Th, respectively (Fig. 11).

679 ## 8. DISCUSSION

680 ### 8.1. C-LVC growth and volume estimate

681 Cross sections depicted in Figure 5 A, B point to hypothetical deep structures inferred from
682 field observations in areas adjacent to the C-LVC west and east of the Western Cordillera. From
683 maximal and minimal elevations (highest and lowest contact points between C-LVC and
684 bedrock; Fig. 5 A and B) measured around all edifices, the basal slope of C-LVC, as observed
685 in the Yura valley to the west and in the Arequipa basin to the SW, dips > 4° towards West and
686 > 5° towards SW and SE. One handicap is the fact that the basal contact surface between the
687 edifices and the bedrock is known only on the edges of the complex (e.g., along the Río Chili
688 canyon). We used three techniques to calculate the volume of C-LVC: (1) a network of x,y,z
689 dots (sampled each 1 km) tracing the exposed contact on the geologic map was integrated on
690 Surfer® software to construct an assumed C-LVC basal surface with the kriging interpolation
691 method. We then determined the volumetric difference between the 30-m DEM of the current
692 surface topography and the calculated basal surface, obtaining a volume of 289 km^3.
693 Intersection points between the profiles (Fig. 5) and calculated surface were also used to build

694 a 3D-block diagram (Fig. 6). With the same principle but using (2) interpolation of Triangular
695 Irregular Networks (TIN) obtained from 30-m DEM data, and reference inclined contact surface
696 between bedrock and C-LVC derived from exposed outcrops, we computed a volume of 346
697 km^3 on ArcMap® software. In addition, (3) considering the volcanoclastic deposits in the
698 western wall of the Río Chili canyon (base of Estribo edifice) and inclined reference basal
699 surface, we obtained a volume as large as 390 km^3 with the NETVOLC (Euillades et al., 2013)
700 and MORVOLC algorithms (Grosse et al., 2012). Thus, we consider the two first estimated
701 values, which are similar within ~60 km^3 as more accurate than the results using NETVOLC
702 and MORVOLC algorithms which deviate significantly from each other (190 - 390 km^3). Table
703 4 shows ~290 (289) – ~350 (346) km^3 the volume estimates for each edifice as well as the
704 eruption rates calculated from the volumes and know ages for each stratigraphic interval.

705 ***8.1.1. Limitations and uncertainties in computing edifice volumes***

706 Uncertainties in computing the edifice volumes stem from poorly constrained parameters and
707 intrinsic limitations: (1) Surface areas are taken from the geologic map (Fig. 4) and 3D-
708 diagrams based on the reconstructed DEM (Fig. 6), while contacts have been derived from
709 exposed outcrops. (2) The thickness of lava piles and domes can only be roughly measured
710 except for the Airport-Potrero dome-coulees cluster and recent lava-flow fields that can be
711 directly measured in the field. (3) The geometry of deep structures beneath the Old Edifice
712 group remains poorly constrained, but the staircase morphology of the SW flank of Western
713 Cordillera (Fig. 6B) and active fault scarps (Río Chili, Aguada Blanca, Fig. 3A) has helped
714 suggest the pre-Chachani palaeo-tropography (Fig. 5), which was used to calculate the volume
715 of the C-LVC. (4) Estimated from the DEM and 3D-diagram (Figs. 4, 6), at least one fifth of
716 the initial volume of the older edifices has been removed either by glaciers, rockslides and
717 debris avalanches (Karátson et al. 2012), as shown by scars open on the SW-facing flanks of
718 the Estribo, El Angel, Chingana and Nocarane stratovolcanoes. (5) The volume of pyroclastic
719 deposits is small compared to lava flows and domes across the C-LVC, due to prevailing
720 effusive and extrusive activity and/or easier erosion of pyroclastic deposits by glaciers. Moraine
721 deposits cover the entire complex above 3800−3900 m in elevation, but an unknown volume of
722 pyroclastic deposits has been removed from the cluster by the Río Chili canyon and SW
723 drainages. Reworked glacial debris and volcaniclastic deposits have been exported out of the
724 cluster to the SW and SE, as shown by volcaniclastic deposits exposed along the walls of the
725 Río Chili canyon, and to the south onto the surface of the ignimbrite infill of the basin of
726 Arequipa. We have computed the area of volcaniclastic deposits on the top of AAI (south ring

727 plain of C-LVC) to be 180 ± 10 km^2. Assigning 20 m for the deposit thickness (varying between
728 10 and 50 m), we estimated the volume to be in the range of 3.40 to 3.80 km^3. The volume of
729 > 50 m-thick volcaniclastic deposits exposed on both walls of the Rio Chili canyon is likely
730 larger. Combined with the volume of deposits onto the top ignimbrite filling the basin, this leads
731 us to estimate, despite the uncertainty in the initial volume (Table 4), that at least 15% of the
732 initial Old Edifice group was removed away.

733 The computed volume of *c.* 63–75 km^3 for Young Edifice magmatism represents 25 to 39 % of
734 the volume estimate of the C-LVC Old Edifice (Table 4). Young Edifice are volumetrically
735 similar to well preserved composite cones of the Middle–Late Pleistocene Frontal arc in south
736 Peru (e.g., Ubinas, Misti and Ampato) and is larger than the ~37 km^3 volume of the
737 Aucanquilcha volcano in Chile that was also built over a period of ~1 Ma (Klemetti and
738 Grunder, 2007). Moreover, the estimated *c.* 290 - 350 km^3 volume of the C-LVC compares
739 well with volumes computed for large regional volcano clusters or fields. For example, the
740 volume of Mount Mazama massif (Oregon, USA) with a 450 ka-long eruptive history is
741 estimated to be 58–112 km^3 (Bacon and Lanphere, 2006), taking into account that C-LVC size
742 and lifetime are twofold to 2.5 times these numbers.

743 **8.2 Eruption rates**

744 Given the limitations in accurately estimating volumes of dated deposits at high spatial and
745 temporal resolution, we can only focus on average, bulk eruption rates for each of the two
746 edifice groups. The Old Edifice eruptive rate, 0.27-0.41 km^3/ka over a 600 kyr period, is in the
747 same order of magnitude than the 0.26-0. 31 km^3/ka entire C-LVC rate averaged over the 1.27
748 My lifetime (Table 4). The Young Edifice group eruptive rate (0.12-0.15 km^3/ka) is 2.5 times
749 lower than that of the Old Edifice group. This is not surprising as (1) Old Edifice group sones
750 (e.g., Nocarane) are twice to three times as large as the most voluminous edifice of the Young
751 Edifice group (e.g., Chachani) and have almost two times higher eruptive rates compared to the
752 Young Edifice group (e.g., Chachani). Since we did not consider glacial erosion on the older
753 edifices, this difference should even be larger. (2) Young edifices, mostly domes and lava fields,
754 have not formed stratovolcanoes, although the youngest Nevado Chachani stratocone is likely
755 the fastest-growing C-LVC composite cone (Table 4), and (3) together with smaller
756 uncertainties in growth duration for domes, dome clusters, and silica-rich, compound ‘aa’ lava
757 fields. We bear in mind that such average eruption rates are highly skewed by the age range
758 over which volumes are integrated: for example, eruption rates of 0.12-0.15 km^3/ka over the
759 460 kyr-long term Young Edifice magmatism are twice as high as the 50-200 kyr-short term

Old Edifice magmatism (0.01-0.03 km^3/ka). The short-term eruption rates of the largest C-LVC edifices (0.35-0.70 km^3/ka) resemble the average growth rate of active composite cones in southern Peru (Thouret et al., 2001; Samaniego et al., 2016) are in accordance with the estimated 0.37 km^3/ka magma eruption rate averaged at the CVZ scale over the past 10 My (Francis and Hawkesworth, 1994). This is comparable to the long-term Mt. Mazama field eruption rate of 0.42 km^3/ka, which stems from the total volume of 176 km^3 magma output in the region over the past 420 kyr (Bacon and Lanphere, 2006). As pointed out by Hildreth and Lanphere (1994), stratovolcanoes commonly grow in "spurts" superimposed on relatively steady and low long-term productivity. Here in C-LVC, only composite cones as recent as Chachani show relatively high eruptive rates (0.27-0.31 km^3/ka) that are comparable to averaged eruptive rates of individual volcanoes, e.g., Ubinas and Sabancaya (Rivera et al., 2014, 2017; Samaniego et al., 2016) in Peru and Parinacota in North Chile (0.25-0.31 km^3/ka, Hora et al., 2007). The eruptive rate over the 112 kyr-long Misti 2-4 stratocone growth with a preserved volume of 73-80 km^3 has been averaged at 0.63 km^3/ka (Thouret et al., 2001), but the Young Edifice group eruption rate is similar to the 0.12 km^3/ka eruptive activity of the Ampato-Sabancaya compound volcano (Tables 1 and 3).

8.3 Petrogenetic processes acting during the C-LVC lifetime

8.3.1 Processes in the deep crust

Compositional changes in time and space have been studied in magmas of the Central Andes (e.g., Mamani et al., 2010; Wörner et al., 2018) in order to determine the relationship between chemical signatures (major and trace elements and isotopic data) and the thickening process of the continental crust. Trace element ratios such as Sr/Y, La/Yb, Sm/Yb and Dy/Yb may indicate the crustal setting where magmatic differentiation (fractional crystallization and/or crustal contamination) occurred. In the Central Andes, maximum Sr/Y and Dy/Yb ratios are observed in intermediate andesites and dacites (55-65 wt.% SiO_2) erupted during the last 5 Ma; even if low values in these ratios can occur at any time (Wörner et al., 2018). However, all C-LVC lavas (53-67 wt.% SiO_2) do not show such maximum or minimum trace element ratios as observed in Quaternary lavas (<2 Ma) in the Central Andes. Sr/Y, Dy/Yb and Sm/Yb ratios in C-LVC vary between 23–71, 1.8–2.8 and 2.2–8 respectively, and these are intermediate values (Fig. 12), compared with the composition of volcanic rocks of similar Pleistocene-Holocene age in the CVZ (Wörner et al., 2018). Such intermediate values argue against a strong garnet signature for the C-LVC magmas. In summary, REE systematics clearly suggest the lower-middle crust fractionation of garnet is probably a minor process during the evolution of C-LVC

magmas. Small differences in Dy/Yb *vs.* Sm/Yb ratios of individual volcanoes in the C-LVC may reflect the compositional variability of the crust and the complexity of the structural setting between the Old- and the Young Edifice groups.

8.3.2 Fractional crystallization, magma mixing, and crustal contamination

The compositional and mineralogical variations in C-LVC lavas through time (See ESD Figs. 2 and 3) can be interpreted as the evolution of the magmatic system controlled by fractional crystallization, assimilation, and magma mixing. Additional processes such as cumulate recycling and remelting may also need to be considered. This interpretation stems from the depletion in compatible elements with increasing silica contents and rather scattered trends in incompatible *vs.* compatible element diagrams (Fig. 13). The two contrasted patterns displayed in Figures 9 and 13 oppose the Old- to the Young Edifice group lava samples, suggesting a progressive change to the homogenization or maturation of the C-LVC magmatic system. Other trace elements (e.g., Rb and Ni) display a similar behavior.

At the same time, an increase in the average phenocrysts content of lavas (< 35 vol.% to generally > 40 vol.%) and a two-fold decrease in magma eruptive rates (from 0.21-0.34 to 0.07-0.09 km^3/ka: Table 4) is documented between the Old- to Young Edifice group. We interpret this observation as an indication that magma residence times increased and (degassing-driven) crystallization and crystal recycling from previous magmatic events increased, suggesting a link between higher crystallinity and lower eruption rate.

Trace element ratios versus silica contents allow us to infer fractional crystallization. In Figure 12A the positive correlation between the Ba/Sr ratio and silica content indicates the fractionation of plagioclase. On the other hand, Dy/Yb ratio decreases slightly with SiO_2 increase (17C), whereas Sr/Y and Sm/Yb ratios display quite scattered values (17B, D). These trends suggest a role of amphibole fractionation during differentiation (Davidson et al., 2007). Decreasing Cr and Ni suggest removal of ferromagnesian minerals such as olivine and pyroxene during the early stages of differentiation. A limited number of samples in Old Edifice group show higher Cr and Ni values than the majority of C-LVC samples, while such high values are correlated with olivine phenocrysts observed in the less differentiated lavas. The negative correlation between Sr and Sc with silica contents point to crystallization of plagioclase and pyroxene during the entire C-LVC lifetime.

In order to test the role of fractional crystallization, in figure 13 we plot a compatible (Ni) against an incompatible element (Rb). The large dispersion observed suggests that fractional

crystallization is insufficient to explain the scattering. In this diagram fractional crystallization of ferromagnesian minerals display a curved trend with a strong decrease of Ni coupled with a weak increase of Rb, for the early fractional crystallization stages, and then a strong increase of Rb (coupled with almost no variation of Ni). Using the mineralogical composition of the cumulate estimated for Ubinas magmatic series (46–48% Pl + 38–44% Amph + 3–5% Cpx + 6% Mag + 1% Apt; Samaniego et al., 2020) and the partition coefficients compiled by Rivera et al. (2017), we estimated a Rayleigh fractional crystallization model using D_{Rb}= 0.05 and D_{Ni}= 4.00 as bulk distribution coefficient values. The comparison of the C-LVC geochemical data; and in a more general the whole CVZ magmas (gray dots and dotted field in Fig. 13) clearly shows that although the C-LVC samples show a global decrease of Ni with Rb increase, these data do not follow the theoretical fractional crystallization trend. In contrasts, mixing process between a primitive (with high Ni and low Rb contents) and a differentiated endmember (with low Ni and high Rb contents) can explain the geochemical variability of C-LVC magmas. These trends indicate complex magmatic processes involving fractional crystallization (coupled with variable crustal assimilation) and frequent magma mixing. This is consistent with the trace elements and isotopic lines of evidence that constrain the crustal contamination in Peruvian volcanoes at around 10-20% at both regional (Mamani et al., 2010; Blum-Oeste and Wörner, 2016) and local scales (Ubinas, Thouret et al., 2005; Samaniego et al., 2020; Misti, Rivera et al., 2017; Ampato-Sabancaya, Gerbe and Thouret, 2004; Samaniego et al., 2016).

8.3.3. Disequilibrium textures as evidence for open system evolution

'Sieve' textures are related to rapid growth, whereas spongy cellular textures (Fig. 7) are commonly attributed to pervasive dissolution (e.g., Ruprecht and Wörner, 2007). The sieve textures can be interpreted as the result of magma mixing, but also from rapid decompression with no substantial heat changes (Nelson and Montana, 1992). Breakdown textures appear when an existing mineral is out of equilibrium and transforms into a new set of minerals instead of dissolving (Streck, 2008). Such textures are observed in most of the C-LVC samples, where the crystal edges are affected, producing reaction rims or generating pseudomorphs. Some amphibole, biotite, orthopyroxene and olivine crystals show sub-rounded or rounded shapes due to dissolution caused by resorption processes. In the C-LVC lava samples, breakdown textures might be produced by pressure decrease and volatile lost during magma ascent.

In summary, the frequent disequilibrium textures observed in plagioclase phenocrysts as well as the chemical variations of plagioclase and amphibole indicate that magma mixing/recharge are prominent processes throughout the entire history of the C-LVC.

858 Based on plagioclase pheno- and microcrysts compositions (see ESD Fig. 2), we argue that
859 fractional crystallization alone would not explain the chemical diversity of C-LVC magmas.
860 We suggest that magma recharge and subsequent mixing or mingling processes also play an
861 important role during the C-LVC evolution. In this context, two non-exclusive models have
862 been proposed in the literature (Couch et al., 2001; Ruprecht and Wörner, 2007): (1) the
863 physical mixing between magmas of contrasting compositions, temperatures and physical
864 properties; and (2) the recharge of a magmatic reservoir by mafic magma, producing an increase
865 in temperature and thus thermal convection, without physical mixing between these magmas.
866 In order to discriminate between these processes, Ruprecht and Wörner (2007) proposed to
867 focus on the systematic variations of anorthite and Fe contents in plagioclase. Given that Fe is
868 a trace element in feldspars, only the melt composition and degree of oxidation may affect Fe
869 content in plagioclase (Ginibre et al., 2002; Ruprecht and Wörner, 2007). Based on this
870 assumption, observed increase in anorthite and Fe in plagioclase may be the result of physical
871 mixing process. In contrast, increase of anorthite values without variation in Fe may result from
872 thermal mixing (or "self-mixing", Couch et al., 2001).

873 Taking the hypotheses based on increasing values in iron and calcium in reverse-zoned
874 plagioclase crystals, we suggest that many analyzed lava samples from Upper Chingana, Lower
875 Nocarane, Upper Estribo, La Torta, Upper Chachani and Volcancillo lavas were affected by
876 compositional mixing (Fig. 14). In contrast, the reverse and/or oscillatory zoning in plagioclase
877 crystals without iron increase in lava samples from El Rodado, La Horqueta, Airport-Potrero
878 Domes and Lower Chachani have recorded thermal mixing, probably due to thermal convection
879 in magma reservoirs.

880 As they have been observed in whole rock geochemistry, differences in plagioclase composition
881 between Old- and Young Edifice lavas are also remarkable. Old Edifice lavas show wider
882 ranges in An_{30-80} and FeO (0.17–1.44 wt.%) values compared to Young Edifice group (An_{29-67}
883 and 0.15–0.72 wt.% FeO), with exception of La Torta dome ($An_{31–64}$ and 0.27–1.42 wt.% FeO),
884 which was emplaced to the north of La Horqueta cumulo dome. Differences in plagioclase and
885 amphibole composition (Fig. 14) might suggest that thermal and compositional mixing and
886 mafic recharge was more frequent processes in magmas emplaced during the Old Edifice group
887 as compared to the Young Edifice group.

888 **8.4 Implications of C-LVC on CVZ magmatic regimes and transcrustal magmatic systems**
889 **in southern Peru**

A model of transcrustal magma feeding systems for the CVZ has been proposed to define three magmatic regimes controlled by the recharge of hotter and less evolved magmas that ascend from depth into shallow reservoirs below arc volcanoes in the Central Andes (Wörner et al., 2018, and Fig. 15). These three regimes are: (1) The accumulation regime (steady state) referred to low recharge rates of the reservoirs over a few of millions of years producing uniform hybrid dacites with slow growth of volcanoes. (2) The activation regime, which consists of increasing mafic recharge that produce higher eruption rates with emission of a wide range of compositions (basaltic andesites to rhyolites) during several hundreds of kyr. (3) The breakthrough regime occurring with high recharge rates producing mafic to intermediate andesites and occurs in the younger edifices during a time span of several kyr.

The C-LVC case study demonstrates that volcanic clusters can experience a shift between steady and unsteady, accumulation and activation regimes. Petrographic differences such as the increase in phenocryst content and maximum crystal size, decrease of An-contents in plagioclase and Ca-content in pyroxene from Old- to Young Edifice group magmas indicate important changes during the long and continuous evolution of C-LVC. The large compositional range and relatively fast eruption rate during the early (> 0.6 Ma) cluster may likely relate to higher rates of mafic recharge and higher contrast in endmember compositions during magma mixing. The narrow compositional range (also observed in most incompatible elements such as Rb, U, Th) and lowering of eruption rate towards the Young Edifice units (< 0.4 Ma) cluster suggests a process of "maturation" towards the younger (and more evolved) magmatic stages. Changes back-and-forth between magmatic regimes depend on the rate of mafic recharges from below and the size and temperature of resident, evolved magmas at shallow levels. The zone of storage, mixing, differentiation and crystallization has not been imaged in the upper crust below the C-LVC, but two independent lines of evidence stem from recent studies that suggested the existence of evolved magmas at shallow depths <15 km.

1. A recent seismological study highlighted the existence of a strong scatter of seismic energy coinciding with a low-velocity zone at a depth of 5−10 km "located at 71.6°W-16.1°S with an error of 10 km beneath the dormant Nevado Chachani and the active El Misti" (Ma et al., 2013). The authors modeled a vertical cylinder about 5 km in diameter that can be interpreted as a low-velocity magma reservoir. This opens the possibility of repeated magma recharges from shallow crustal depths compatible with recent thermo-barometric calculations on El Misti magmas (Tepley et al., 2013; Rivera et al., 2017).

2. Mafic magma recharge and subsequent magma mixing under arc volcanoes around the C-LVC have been suggested by studies of disequilibrium textures and mineral chemistry of eruptive products recently erupted at Sabancaya (Gerbe and Thouret, 2004), Ubinas (Thouret et al., 2005; Rivera et al., 2017; Samaniego et al., 2020) and Tutupaca (Manrique et al., 2020). The depth of magma reservoirs has been estimated in the range of 9 to 15 km below the craters of El Misti (Rivera et al., 2017) and Ubinas (Rivera et al., 2014; Samaniego et al., 2020); a spherical-shape deformation source was identified at 11-14 km north of Sabancaya volcano below the Hualca Hualca volcano during the ongoing eruptive period that started in November 2016 (Cruz, 2019). The temporal evolution towards more uniform and evolved composition, and the petrology dataset (see section 7) support the hypothesis that the long-lived C-LVC represents a long-lived and slowly evolving transcrustal magma system. The compositional variety of magmas in the Old Edifice group suggests increased but variable recharges from below into the shallow reservoir.

This thermally 'alive' upper crust may have prevailed further back since early Pleistocene time, as the 1.28, 1.40, and 1.62−1.66 Ma ignimbrite eruptions point to the absence of any protracted lull in the eruptive activity in the region in which the C-LVC has grown. Interesting questions arise from the close temporal relation between the ignimbrite eruptions directly preceding the onset of eruptions at the C-LVC. Intense eruptions of silicic magma are recorded by the Yura Tuffs and the Arequipa Airport ignimbrite between 1.66 and 1.28 Ma, i.e., immediately before the onset of magmatic activity at the Chachani cluster (<1.28 Ma). How are these magmatic systems related? Is the C-LVC a dying magmatic system that followed a larger silicic magma reservoir that fed the ignimbrites? Does the focus of magmatism change in depth with time? Or is there a change from silicic magma ponding during the ignimbrite stage followed by: increasing recharge rates that resulted in a "break-through" of mafic recharge magmas and increased mixing and reactivation of older crystal-rich magmas in a mushy transcrustal reservoir? These questions need to be addressed by further analytical work focusing in particular on compositional variations and zonations on phenocryst minerals and diffusion speedometry of magmatic processes.

CONCLUDING REMARKS

The evolution of the Chachani large volcanic cluster (C-LVC) reveals how these long-lived volcanic structures grow from transcrustal magma systems in the CVZ and why magmatic

regimes have shifted from initial large compositional variations to steady state, monotonous andesitic regime through the *c.* 1.28 Myr cluster lifetime.

1.Twelve volcanic edifices overlying the Pre-Chachani lavas (>1278 ka) have formed (i) the Early to Middle Pleistocene Old Edifice group (<1100–640 ka) with a relatively large range from basaltic andesite to dacite compositions (53-67 wt.% SiO_2), and (ii) the middle to late Pleistocene group (>400–56 ka) of Young Edifice domes and dome-coulee complexes, stratocones and lava flow fields showing a narrower range of andesitic and minor dacitic compositions (58-64 wt.% SiO_2).

2. The volume of each of the C-LVC edifices has been estimated despite a number of uncertainties. The DEM-based calculations yielded a 289 and 346 ± 29/35 km^3 range. The Old Edifice group represent two thirds of the C-LVC volume, whereas the Young Edifice volume represents about the remaining one third of the estimated volume. Young edifices are volumetrically similar to young, weakly eroded stratocones of the frontal arc in southern Peru.

3. Slow bulk eruption rates estimated for both groups of edifices are similar to comparable CVZ long-lived clusters (e.g., Aucanquilcha, North Chile) or elsewhere (e.g., Mt. Mazama and Crater Lake volcanic centres, Cascades). Eruptive rates have slowed down twofold from Old Edifice (0.27-0.41 km^3/ka) to Young Edifice C-LVC (0.12-0.15 km^3/ka), coinciding with monotonous andesitic compositions. This suggests that the C-LVC magmatic system became mature with time. This means that slow but constant eruptive rates feeding Young Edifice magmatism produced uniform, evolved compositions by continuous mafic recharge, magma mixing and thermal stabilization. A similar, stable magmatic system with uniform erupted magma compositions and evidence for long-lasting temperature cycling of the magma reservoir was documented for the dacitic Taápaca volcano in North Chile (Rout and Wörner, 2021).

4. Bulk rock major and trace elements highlight the fact that C-LVC compositions have varied along three different periods: following homogeneous compositional range of the Pre-Chachani and Chachani base lava flows, the range expands in lavas of the Old Edifice group, but the compositions narrowed and became relatively homogeneous in the Young Edifice lavas. This suggests changes in magma source location and/or repeated magma recharge and thermal pulses.

5. Bulk rock and mineral chemical analyses suggest that the C-LVC represents protracted post-caldera activity, which directly followed the 1.62-1.66 Ma Arequipa Airport ignimbrite. This confirms the genetic link between this medium-sized ignimbrite event and the subsequent

evolution of the C-LVC thus significantly expanding the lifetime and volume of this magmatic system.

6. Mineral disequilibrium textures and composition changes support frequent recharge events during the C-LVC lifetime. FeO–An systematics used in plagioclase crystals indicate compositional mixing or mingling in samples of the late events during Old- and in the Young Edifice magmatism.

Acknowledgments

We thank the Editor, K. Russell, and reviewers E. Klemetti and D. Karátson for their comments and constructive suggestions made on the early version of the manuscript, which helped to improve its content. This work stems from the first author's Master study hosted at the Laboratoire Magmas et Volcans in Clermont-Ferrand with the support of the French Centre National de Recherche Scientifique and Institut de Recherche pour le Développement. The initial internship work was supported by the Réseau inter-universitaire R. Porras Barrenechea of the French Embassy in Peru. Part of the sampling and analytical work of G.W. was supported by the German Science Foundation grant Wo362/31-1. We thank late H. Martin, V. Carlotto and INGEMMET for administrative support in France and Peru, M. Benbakkar for ICP-AES analyses, J.L. Devidal for microprobe analyses, P. Grosse for helping us using the MORVOLC software, E. Romero for field assistance, and the LMV technical staff in particular C. Fonquernie for continuous support in laboratory analyses.

References

Aguilar, R., 2015. Long-lived magmatic systems: the post-caldera Chachani volcanic complex case study, Peru. MSc report (Unpubl.), Laboratoire Magmas et Volcans, Université Clermont-Auvergne, Clermont-Ferrand

Armijo, R., Lacassin, R., Coudurier-Curveur, A., Carrizo, D., 2015. Coupled tectonic evolution of Andean orogeny and global climate. Earth-Sci Rev 143: 1–35

Bacon, C., Lanphere, M., 2006. Eruptive history and geochronology of Mount Mazama and the Crater Lake region. Geol Soc Amer Bull 118(11/12): 1331-1359

1015 Benavente, C., Delgado, F., García, B., Aguirre, E., Audin, L., 2017. Neotectónica, Evolución
1016 y Peligro Sísmico en la Región Arequipa. INGEMMET, Boletín Serie C: Geodinámica e
1017 Ingeniería Geológica N° 64, 395 pp

1018 Benavides-Cáceres, V., 1999. The Andean cycle. In: Skinner BJ (ed.), Geology and ore
1019 deposits of the Central Andes. Soc Eco Geol Spec Publ 7: 61-107

1020 Bernard. K., Thouret, J.-C., Van Wyk de Vries, B., 2017. Emplacement and transformations
1021 of volcanic debris avalanches – A case study at El Misti volcano, Peru. J Volcanol Geotherm
1022 Res 340: 68-91

1023 Blum-Oeste, M., Wörner, G., 2016. Central Andean magmatism can be constrained by three
1024 ubiquitous end-members. Terra Nova: 1-7, doi: 10.1111/ter.12237

1025 Bromley, G., Thouret, J-C, Schimmelpfennig, I., Mariño, J., Valdivia, D., Rademaker, T.,
1026 Vivanco Lopez SdP., ASTER Team, Aumaître, G., Bourlès, D., Keddadouche, K., 2019. In
1027 situ cosmo-genic ^{3}He and ^{36}Cl and radiocarbon dating of volcanic deposits refine the
1028 Pleistocene and Holocene eruption chronology of SW Peru. Bull Volc 81: 64

1029 Carlotto, V., Quispe, J., Acosta, H., Rodríguez, R., Romero, D., Cerpa, L., Mamani, M., Díaz-
1030 Martínez, E., Navarro, P., Jaimes, F., Velarde, T., Lu, S., Cueva, E., 2009. Dominios
1031 geotectónicos y metalogénesis del Perú. Bol Soc Geol Perú 103: 1-89

1032 Clavero, J.E., Sparks, R.S.J., Pringle, M.S., Polanco, E., Gardeweg, M.C., 2004. Evolution and
1033 volcanic hazards of Taápaca Volcanic Complex, Central Andes of Northern Chile. J Geol Soc
1034 London 161: 603-618, doi.org/10.1144/0016-764902-065

1035 Coombs, M.L., Jicha, B.R., 2021. The eruptive history, magmatic evolution, and influence of
1036 glacial ice at long-lived Akutan volcano, eastern Aleutian Islands, Alaska, USA. Geol Soc
1037 Amer Bull 133 (5-6): 963–991

1038 Couch, S., Sparks, R.S.J., Carroll, M.R., 2001. Mineral disequilibrium in lavas explained by
1039 convective self-mixing in open magma chambers. Nature 411: 1037–1039

1040 Cruz, L., 2019. Análisis de deformación del volcán Sabancaya como herramienta útil en el
1041 pronóstico de erupciones periodo 2012–2017. Tesis de grado Universidad Nacional San
1042 Agustín, Arequipa

1043 Davidson, J.P., Turner, S., Handley, H., Macpherson, C., Dosseto, A., 2007. Amphibole
1044 "sponge" in arc crust? Geology 35(9): 787, doi:10.1130/g23637a.1

1045 Davidson, J.P., McMillan, N.J.M., Moorbath, S., Wörner, G., Harmon, R.S., Lopez-Escobar,
1046 L., 1990. The Nevados de Payachata volcanic region (18°S/69°W, N Chile). II. Evidence for
1047 widespread crustal involvement in Andean magmatism. Contrib Mineral Petrol 105: 412-432.

1048 Davidson, J.P., Harmon, R.S., Wörner, G., 1991. The source of Central Andean magmas; some
1049 considerations. In: Harmon RS, Rapela CW (eds) Andean Magmatism and its tectonic setting.
1050 Geol Soc Amer Spec Paper 265: 233-244

1051 Delacour, A., Gerbe, M.-C., Thouret, J.-C., Wörner, G., Paquereau, P., 2007. Magma evolution
1052 of Quaternary minor volcanic centres in Southern Peru, Central Andes. Bull Volc 69, 6: 581-
1053 606

1054 de Silva, S.L., Kay, S.M. (2018) Turning up the heat: High-flux magmatism in the Central
1055 Andes. Elements 14: 245-250. DOI: 10.2138/gselements.14.4.245

1056 Feeley, T.C., Davidson, J.P., Armendia, A., 1993. The volcanic and magmatic evolution of
1057 Volcan Ollaguë, a high-K, late Quaternary stratovolcano in the Andean Central Volcanic
1058 Zone. J Volc Geoth Res 54: 221-245

1059 Feeley, T.C., Davidson, J.P., 1994. Petrology of calc-alkaline lavas at Volcán Ollaguë and the
1060 origin of compositional diversity at Central Andean stratovolcanoes. J Petrol 35: 1295–1340

1061 Francis, P.W., 1993. Volcanoes. A Planetary Perspective: Oxford University Press, 443 pp

1062 Francis PW, Hawksworth CJ (1994) Late Cenozoic rates of magmatic activity in the Central
1063 Andes and their relationships to continental crust formation and thickening. J Geol Soc
1064 London 151: 845–854

1065 Froger, J.L., Remy, D., Bonvalot, S., Legrand, D., 2007. Two scales of inflation at Lastarria-
1066 Cordon del Azufre volcanic complex, central Andes, revealed from ASAR-ENVISAT
1067 interferometric data. Earth Planet Sci Lett 255, 1-2: 148-163

1068 Garcia, F., Chorowicz, J., Legros, F., 1997. La caldera Chachani, gran centro explosivo
1069 Plioceno-Holoceno del sur del Perú? Identificación y evolución en imagenes Landsat y Radar
1070 ERS. Soc Geol Perú, vol esp 1: 449-454

1071 Gardeweg, M.C., Sparks, R.S.J., Matthews, S.J., 1998. Evolution of Lascar volcano, Northern
1072 Chile. J Geol Soc London 155: 89-104

1073 Gerbe, M.C., Thouret, J.-C., 2004. Role of magma mixing in the petrogenesis of lavas erupted
1074 through the 1990–98 explosive activity of Nevado Sabancaya in south Peru. Bull Volcanol
1075 66, 541–561

1076 Ginibre, C., Kronz, A., Wörner, G., 2002. High resolution quantitative imaging of plagioclase
1077 composition using accumulated back scattered electron images: new constraints on oscillatory
1078 zoning. Contrib Mineral Petrol 142: 436-448

1079 Godoy, B., Wörner, G., Kojima, S., Aguilera, F., Simon, K., Hartmann, G., 2014. Low pressure
1080 evolution of arc magmas in thickened crust: the San Pedro-Linzor volcanic chain, Central
1081 Andes, Northern Chile. J South Amer Earth Sci 52: 24-42

1082 Gonzales, K., Finizola, A., Lénat, J.-F., Macedo, O., Ramos, D., Thouret, J.-C., Fournier, N.,
1083 Cruz, V., Pistre, K., 2014. Asymmetrical structure, hydrothermal system and edifice stability:
1084 The case of Ubinas volcano, Peru, revealed by geophysical surveys. J Volc Geoth Res 276:
1085 132–144

1086 Grosse, P., Euillades, P.A., Euillades, L.D., Van Wyk de Vries, B., 2013. A global database of
1087 volcano morphometry. Bull Volc 76, 784 DOI 10.1007/s00445-013-0784-4

1088 Grosse, P, van Wyk de Vries, B, Euillades, PA, Kervyn, M, Petrinovic, IA, 2012. Systematic
1089 morphometric characterization of volcanic edifices using digital elevation models.
1090 Geomorphology, 136: 114-131

1091 Grosse, P., van Wyk de Vries, B., Petrinovic, I.A., Euillades, P.A., Alvarado, G., 2009.
1092 Morphometry and evolution of arc volcanoes. Geology 37, 651–654.

1093 Grunder, A.L., Klemetti, E.W., Feeley, T.C., McKee, C.M., 2008. Eleven million years of arc
1094 volcanism at the Aucanquilcha Volcanic Cluster, Northern Chilean Andes: implications for
1095 the life span and emplacement of plutons. Trans Royal Soc Edinburgh-Earth Sci 97: 415-436

1096 Guevara, C., 1969. Geología del cuandrángulo de Characato. Servicio de Geología y Minería,
1097 Bol. 23, 53 p., color map 1: 100 000, Lima

1098 Harpel, C., da Silva, S., Salas, G., 2011. The 2-ka eruption of Misti volcano, southern Peru -
1099 The most recent plinian eruption of Arequipa's iconic volcano. Geol Soc Amer Spec Paper
1100 484: 1-72

1101 Hildreth, W., Lanphere, M.A., 1994. Postassium-Argon geochronology of a basalt-andesite-
1102 dacite arc system—The Mount Adams volcanic field, Cascade Range of Western
1103 Washington. Geol Soc Amer Bull 106: 1413-1429

1104 Hildreth, W., Fierstein, J., Lanphere, M.A., 2003. Eruptive history and geochronology of the
1105 Mount Baker volcanic field, Washington. Geol Soc Am Bull 115: 729–764

1106 Hora, J.M., Singer, B., Wörner, G., 2007. Volcano evolution and eruptive flux on the thick crust
1107 of the Andean Central Volcanic Zone: $^{40}Ar/^{39}$ Ar constraints from Volcán Parinacota, Chile.
1108 Geol Soc Amer Bull 119, 3/4: 343-362

1109 Hoshizumi., H., Uto, K., Watanabe, K., 1999. Geology and eruptive history of Unzen Volcano,
1110 Shimabara Peninsula, Kyushu, SW Japan. J Volc Geoth Res 89, 1–4: 81–94

1111 Hurai, V., Paquette, J.L., Huraiová, M., Konecny, P., 2010. Age of deep crustal magmatic
1112 chambers in the intra-Carpathian back-arc basin inferred from LA-ICPMS U-Th-Pb dating of
1113 zircon and monazite from igneous xenoliths in alkali basalts. J Volc Geoth Res 198:275-287

1114 James, D.E., 1982. A combined O, Sr, Nd and Pb isotopic and trace element study of crustal
1115 contamination in central Andean lavas. I: Local geochemical variations. Earth and Planetary
1116 Science Letters, 57: 47-62, doi.10.1016/0012-821X(82)90172-8

1117 James, D.E., Sacks, I.S., 1999. Cenozoic formation of the Central Andes: A geophysical
1118 perspective, *in* Skinner, B.J., ed., Geology and Ore Deposits of the Central Andes. Society of
1119 Economic Geologists Special Publication, 7: 1-25

1120 Jenks, W., 1948. Geología de la hoja de Arequipa a escala 200 000. Boletín 9, Carta Nacional,
1121 Lima, Peru

1122 Jicha, B.R., Rhodes, J.M., Singer, B.S., Garcia, M.O., 2012. $^{40}Ar/^{39}Ar$ geochronology of
1123 submarine Mauna Loa volcano, Hawaii. J Geophys Res 117: B09204,
1124 doi:10.1029/2012JB009373

1125 Karátson, D., Telbisz T., Worner, G., 2012. Erosion rates and erosion patterns of Neogene to
1126 Quaternary stratovolcanoes in the Western Cordillera of the Central Andes: An SRTM DEM
1127 based analysis. Geomorph 139-140: 122-135

1128 Klemetti, E.K., Grunder, A.L., 2007. Volcanic evolution of Volcán Aucanquilcha, a long-lived,
1129 monotonous dacite volcano in the Central Andes of Northern Chile. Bull Volc 70: 633-650.
1130 Doi 10.1007/s00445-007-0158-x

1131 Kuiper, K.F., Deino, A., Hilgen, F.J., Krijgsman, W., Renne, P.R., Wijbrans, J.R., 2008.
1132 Synchronizing Rock Clocks of Earth History. Science 320: 500-504

1133 Ludwig, K.R., 2001. Users' manual for Isoplot/Ex rev. 2.49. Berkeley geochronology centre,
1134 Special Publ 1a, 55

1135 Ma, Y., Clayton, R.W., Tsai, V.C., Zhan, Z., 2013. Locating a scatterer in the active volcanic
1136 area of Southern Peru from ambient noise cross-correlation. Geophys J Internat 192(3): 1332–
1137 1341. doi:10.1093/gji/ggs103

1138 Mamani, M., Tassara, A., Wörner, G., 2008. Composition and structural control of crustal
1139 domains in the central Andes. Geochem Geophy Geosys 9: 1-13

1140 Mamani, M., Wörner, G., Semperé, T., 2010. Geochemical variation in igneous rocks of the
1141 Central Andean orocline (13 °S to 18 °S): tracing crustal thickening and magmas generation
1142 through time and space. Geol Soc Amer Bull 97: 241–254

1143 Manrique, N., Samaniego, P., Médard, E., Schiavi, F., Marino, J., Liorzou, C., 2020. Pre-
1144 eruptive magmatic processes associated with the historical (218 ±14 a BP) explosive eruption
1145 of Tutupaca volcano (southern Peru). Bull Volc 82:6, doi.org/10.1007/s00445-019-1335-4

1146 Mariño, J., Samaniego, P., Manrique, N., Valderrama, P., Roche, O., Van Wyk de Vries, B.,
1147 Guillou, H., Zerathe, S., Arias, C., Liorzou, C., 2021. The Tutupaca volcanic complex
1148 (Southern Peru): Eruptive chronology and successive destabilization of a dacitic dome
1149 complex. J South Amer Earth Sci 109, 103227, doi.org/10.1016/j.jsames.2021.103227

1150 Mariño, J., Thouret, J.C., Cabrera, M., Aguilar, R., Manrique, N., Edwards, B., Kochtitzky, W.,
1151 2020. Geología y evaluación de los peligros del complejo volcánico Nevado Coropuna.
1152 Boletín Geológico, INGEMMET, Lima: 145 pp

1153 Mathews, S.J., Jones, A.P., Gardeweg, M.C., 1994. Lascar volcano, northern Chile: evidence
1154 for steady-state disequilibrium. J Petrol 35: 401–432

1155 Mering, C., Huaman-Rodrigo, D., Chorowicz, J., Deffontaines, B., Guillande, R., 1996. New
1156 data on the geodynamics of southern Peru from computerized analysis of SPOT and SAR
1157 ERS-1 images. Tectonophys 259: 153–169

1158 Meyers, S.R., Siewert, S.E., Singer, B.S., Sageman, B.B., Condon, D.J., Obradovich, J.D.,
1159 Jicha, B.R., Sawyer, D.A., 2012. Intercalibration of radioisotopic and astrochrono-logic time
1160 scales for the Cenomanian–Turonian boundary interval, Western Interior Basin, USA.
1161 Geology 40: 7–10

1162 Min, K., Mundil, R., Renne, P.R., Ludwig, K.R., 2000. A test for systematic errors in $^{40}Ar/^{39}Ar$
1163 geochronology through comparison with U/Pb analysis of a 1.1-Ga rhyolite. Geochim.
1164 Cosmochim. Acta 64: 73-98

1165 Muir, D.D., Barfod, D.N., Blundy, J.D., Rust, A.C., Sparks, R.S.J., Clarke, K.M., 2015. The
1166 temporal record of magmatism at Cerro Uturuncu, Bolivian Altiplano. In: Carrichi L, Blundy
1167 JD (eds), Chemical, physical and temporal evolution of magmatic systems 422, 1, Geol Soc
1168 London Spec Publ: 57-82

1169 Mullen, E., Paquette, J.L., Tepper, J.H., McCallum, I.S., 2018. Temporal and spatial evolution
1170 of Northern Cascade Arc magmatism revealed by LA–ICP–MS U–Pb zircon dating. Canad J
1171 Earth Sci 55: 443-462, doi:10.1139/cjes-2017-0167

1172 Naranjo, J.A., 1992. Chemistry and petrological evolution of the Lastarria volcanic complex in
1173 the north Chilean Andes. Geol Mag 129: 723-740

1174 Nelson, S.T., Montana, A., 1992. Sieved textured plagioclase in volcanic rocks produced by
1175 rapid decompression. Amer Mineral 77: 1242-1249

1176 O'Callaghan, L.J., Francis, P.W., 1986. Volcanological and petrological evolution of San Pedro
1177 volcano, Provincia El Lao, North Chile. J Geol Soc London 143, 2: 275-286

1178 Ownby, S., Delgado Granados, H., Lange, R.A., Hall, C.M., 2007. Volcán Tancítaro,
1179 Michoacán, Mexico, $^{40}Ar/^{39}Ar$ constraints on its history of sector collapse. J Volc Geoth Res
1180 161: 1–14

1181 Paquereau-Lebti, P., Thouret, J.-C., Wörner, G., Fornari, M., 2006. Neogene and Quaternary
1182 ignimbrites in the area of Arequipa, Southern Peru: Stratigraphical and petrological
1183 correlations. J Volc Geoth Res 154: 251–275, Doi 10.1016/j.jvolgeores.2006.02.014

1184 Paquereau-Lebti, P., Fornari, M., Roperch, P., Thouret, J.-C., Macedo, O., 2008.
1185 Paleomagnetic, magnetic fabric properties, and $^{40}Ar/^{39}Ar$ dating, of Neogene - Quaternary
1186 ignimbrites in the Arequipa area, Southern Peru. Flow directions and implications for the
1187 emplacement mechanisms. Bull Volc 70: 977-997

1188 Paquette, J.L., Piro, J.L., Devidal, J.L., Bosse, V., Didier, A., Sannac, S., Abdelnour, Y., 2014.
1189 Sensitivity enhancement in LA-ICP-MS by N2 addition to carrier gas: Application to
1190 radiometric dating of U-Th-bearing minerals. Agilent ICP-MS J 58, 4–5

1191 Peccerillo, A., Taylor, S.R., 1976. Geochemistry of Eocene calc-alkaline volcanic rocks from
1192 the Kastamonu area, northern Turkey. Contrib Mineral Petrol 58: 63-81

1193 Ramos, V., 2008. The basement of the Central Andes: The Arequipa and related terranes. Ann
1194 Rev Earth Planet Sci 36, 289-324

1195 Ramos, V., 2010. The tectonic regime along the Andes: present-day and Mesozoic regimes.
1196 Geol J 45, 1: 2–25, doi.org/10.1002/gj.1193

1197 Richards, J.P., Villeneuve, M., 2001. The Llullaillaco volcano, Northwest Argentina:
1198 construction by Pleistocene volcanism and destruction by sector collapse. J Volc Geoth Res
1199 105: 77–105

1200 Rivera, M., Thouret, J.-C., Samaniego, P., 2014. The 2006-2008 eruptive products of Ubinas
1201 volcano, Peru: characteristics and implications on eruptive dynamics, magma production and
1202 hazards. J Volc Geoth Res 270: 122-141

1203 Rivera, M., Martin, H., Le Pennec, J.-L., Thouret, J.-C., 2017. Petro-geochemical constraints
1204 on the source and evolution of magmas at El Misti volcano (Peru). Lithos 268-271: 240-259

1205 Robin, C., Samaniego, P., Le Pennec, J.-L., Fornari, M., Mothes, P., van der Plicht, J., 2010.
1206 New radiometric and petrological constraints on the evolution of the Pichincha volcanic
1207 complex (Ecuador). Bull Volc 72: 1109–1129, doi.org/10.1007/s00445-010-0389-0

1208 Rout, S.S., Wörner, G., 2021. Long-term temperature cycling in a shallow magma reservoir:
1209 insights from sanidine megacrysts at Taápaca volcano, Central Andes. J Petrol, egab010,
1210 doi.org/10.109.3/petrology/egab010

1211 Ruprecht, P., Wörner, G., 2007. Variable regimes in magma systems documented in plagioclase
1212 zoning patterns: El Misti strato-volcano and Andahua monogenetic cones. J Volc Geoth Res
1213 165: 142–162

1214 Rutherford, M.J., Hill, P., 1993. Magma ascent rates from amphibole breakdown: an
1215 experimental study applied to the 1980–1986 Mount St. Helens eruptions. J Geoph Res
1216 98:19667–19685, doi: 10.1029/93JB01613

1217 Samaniego, P., Rivera, M., Manrique, N., Schiavi, F., Nauret, F., et al., 2020. Linking magmatic
1218 processes and magma chemistry during the post-glacial to recent explosive eruptions of
1219 Ubinas volcano (southern Peru). J Volc Geoth Res 407: 107095,
1220 doi.org/10.1016/j.jvolgeores.2020.107095

1221 Samaniego, P., Robin, C., Chazot, G., Bourdon, E., Cotton, J., 2010. Evolving metasomatic
1222 agent in the Northern Andean subduction zone, deduced from magma composition of the long-
1223 lived Pichincha volcanic complex (Ecuador). Contrib Mineral Petrol 160:239-260, doi:
1224 10.1007/s00410-009-0475-5

1225 Samaniego, P., Rivera, M., Mariño, J., Guillou, H., Liorzou, C., Zerathe, S., Delgado, R.,
1226 Valderrama, P., Scao, V., 2016. The eruptive chronology of the Ampato-Sabancaya volcanic
1227 complex (southern Peru). J Volc Geoth Res 323: 110–128

1228 Schärer, U., 1984. The effect of initial 230Th disequilibrium on young U-Pb ages: the Makalu
1229 case, Himalaya. Earth Planet. Sci. Lett. 67(2): 191–204, doi:10.1016/0012-821X(84)90114-6

1230 Sempere, T., Jacay, J., 2006. Estructura tectónica del Sur del Perú (Antearco, arco y Altiplano
1231 suroccidental). XIII Congreso Peruano de Geología, Extended Abstracts, Lima: 324-327

1232 Sempere, T., Noury, M., Garcia, F., Bernet, M., 2014. Elementos para una actualización de la
1233 estratigrafia del Grupo Moquegua, sur del Perú. In: XVII Congreso Peruano de Geología,
1234 Lima, Extended Abstracts, digital file "Sempere, T", Soc Geol Perú, Lima

1235 Singer, B.S., Thompson, R.A., Dungan, M.A., Feeley, T.C., Nelson, S.T., Pickens, J.C., Brown,
1236 L.L., Wulff, A.W., Davidson, J.P., Metzger, J., 1997. Volcanism and erosion during the past
1237 930 k.y. at the Tatara-San Pedro complex, Chilean Andes 36º S. Geol Soc Amer Bull 109:
1238 127-142

1239 Sparks, R.S.J., Folkes, C.B., Humphreys, M.C.S., Barfod, D.N., Clavero, J., Sunagua, M.C.,
1240 McNutt, S.R., Pritchard, M.E., 2008. Uturuncu volcano, Bolivia: Volcanic unrest due to
1241 midcrustal magma intrusion. Am J Sci 308, 6: 727-769

1242 Stern, C.R., 2004. Active Andean volcanism: its geologic and tectonic setting. Rev Geol Chile
1243 31, 2: 161-206

1244 Streck. M.J., 2008. Mineral textures and zoning as evidence for open system processes. Rev in
1245 Mineral 69, 595–622

1246 Suaña, E., 2011. Estudio Geológico del Complejo Volcánico Chachani, Arequipa-Perú. Tesis
1247 de grado. Universidad Nacional San Agustín, Arequipa, 302 pp

1248 Sun, S., McDonough, W.F., 1989. Chemical and Isotopic Systematics of Oceanic Basalts:
1249 Implications for Mantle Composition and Processes. Magmatism in the Ocean Basin. Geol
1250 Soc Amer Spec Paper 42: 313–345

1251 Tepley, F.J., de Silva, S., Salas, G., 2013. Magma dynamics and petrological evolution
1252 leading to the VEI 5 2000 BP eruption of El Misti volcano, southern Peru. J Pet 54, 10: 2033–
1253 2065

1254 Tera, F., Wasserburg, G.J., 1972. U–Th–Pb systematics in three Apollo 14 basalts and the
1255 problem of initial Pb in lunar rocks. Earth Planet. Sci. Lett. 14, 281–304

1256 Thorpe, R.S., Francis, P.W., Hammil, M., Baker, M.B., 1982. The Andes, In: Thorpe RS (Ed.),
1257 Andesites, pp. 187–205

1258 Thouret, J.-C., Finizola, A., Fornari, M., Legeley-Padovani, A., Suni, J., Frechen, M., 2001.
1259 Geology of El Misti volcano near the city of Arequipa, Peru. Geol Soc Amer Bull 113, 12:
1260 1593–1610

1261 Thouret, J.-C., Dávila, J., Juvigné, E., Gourgaud, A., Boivin, P., 2002. Reconstruction of the
1262 AD 1600 explosive eruption at Huaynaputina volcano, Peru, based on geologic evidence and
1263 Spanish chronicles. J Volc Geoth Res 115, 3-4: 529-570

1264 Thouret, J.-C., Rivera, M., Wörner, G., Gerbe, M.-C., Finizola, A., Fornari, M., Gonzales, K.,
1265 2005. Ubinas: evolution of the historically most active volcano in Southern Peru. Bull Volc
1266 67: 557-589

1267 Thouret, J.-C., Wörner, G., Singer, B., Gunnell, Y., Zhang, X., Souriot, T., 2007.
1268 Geochronologic and stratigraphic constraints on canyon incision and Miocene uplift of the
1269 Central Andes in Peru. Earth Planet Sci Lett 263:151-166

1270 Thouret, J.C., Mamani, M., Wörner, G., Paquereau-Lebti, P., Gerbe, M.-C., Delacour, A.,
1271 Juvigné, E., Rivera, M., Mariño, J., Cacya, L., Singer, B., 2008. Neogene ignimbrites and
1272 volcanic edifices in southern Peru: stratigraphy, time-volume-composition relationships, and
1273 recent tephra-chronology. 7th International Symposium Andean Geodynamics ISAG, 2-4
1274 September 2008, Nice, Extended Abstracts: 545-548

1275 Thouret, J.-C., Jicha, B., Paquette, J.-L., Cubukcu, E., 2016. A 25 Myr chronostratigraphy of
1276 ignimbrites in South Peru. Implications for the volcanic history of the Central Andes. J Geol
1277 Soc London 173: 734-756, doi: 10.1144/jgs2015-162

1278 Thouret, J.-C., Gunnell, Y., Jicha, B., Paquette, J.-L., Braucher, R., 2017. Canyon incision
1279 chronology based on ignimbrite stratigraphy and cut-and-fill sediment sequences in SW Peru
1280 documents intermittent uplift of the western Central Andes. Geomorph 298: 1-19

1281 Tosdal, R.M., Farrar, E., Clark, A.H., 1981. K-Ar geochronology of the late Cenozoic volcanic
1282 rocks of the Cordillera Occidental, southernmost Peru. J Volc Geoth Res 10: 157-173, doi:
1283 10.1016/0377-0273(81)90060-3

1284 Van Achterbergh, E., Ryan, C.G., Jackson, S.E., Griffin, W.L., 2001. Data reduction software
1285 for LA-ICP-MS (appendix), In : Sylvester PJ (ed.), Laser Ablation –ICP-Mass Spectrometry
1286 in the Earth Sciences: Principles and Applications, Miner Assoc Canada Short Course Series,
1287 Ottawa, Ontario, Canada, 29, 239-243

1288 Vicente, J.-C., Sequeiros, F., Valdivia, M., Zavala, J., 1982. El sobre-escurrimiento de Cincha-
1289 Lluta: elemento del accidente mayor andino al NW de Arequipa. Bol Soc Geol Perú 61: 67-
1290 99

1291 Walker, B.A., Klemetti, E.W., Grunder, A.L., Dilles, J.H., Tepley, F.J., Giles, D., 2013.
1292 Crystal reaming during the assembly, maturation, and waning of an eleven-million-year
1293 crustal magma cycle: thermobarometry of the Aucanquilcha Volcanic Cluster**.** Contrib
1294 Mineral Petrol 165, 4: 663-682, doi: 10.1007/s00410-012-0829-2

1295 Wegner, W., Ruprecht, P., 2003. Volcanic Geology and Valley History of Rio Chili Canyon,
1296 Arequipa (Southern Peru). Diploma Mapping Thesis, University Göttingen (unpubl.): 83 pp

1297 Wilson, J.J., García, W., 1962. Geología de los cuadrángulos de Pachía y Palca. Com. Carta
1298 Geol. Nac., Boletín, 4, 81 p.

1299 Wilson, M., 1986. Igneous petrogenesis: Unwyn Hyman, London, 456 pp

1300 Wörner, G., Harmon, R.S., Davidson, J.P., Moorbath, S., 1988. The Nevados de Payachata
1301 volcanic region 18°S/69°W, N. Chile). I. Geological, geochemical, and isotopic observations.
1302 Bull Volcanol 30: 287-303

1303 Wörner, G., Mamani, M., Blum-Oeste, M., 2018. Magmatism in the Central Andes. Elements
1304 14: 237-244. Doi: 10.2138/gselements.14.4.237

1305

1306 **Tables captions**

1307 **Table 1.** Characteristics of large volcanic clusters (LVCs) and comparison with compound
1308 volcanoes and individual composite stratocones in the Andean CVZ and elsewhere.

1309 **Table 2**. $^{40}Ar/^{39}Ar$ and U/Pb ages of the large Chachani volcano cluster C-LVC and the
1310 neighbouring Yura tuffs.

1311 **Table 3.** Summary of growth stages, eruptive rates, mineral assemblages, and Si02, K20
1312 content in lavas from the C-LVC.

Table 4. Results of calculation using morphometric parameters for the C-LVC and each of its edifices.

Table 5. Petrographic characteristics of lavas from the twelve C-LVC edifices, and of Pre-Chachani and Chachani base lavas. Pl: plagioclase, opx: orthopyroxene, cpx: clinopyroxene, amph: amphibole, bi: biotite, mgt: magnetite. % values in parentheses represents the percentage of crystal content as phenocrysts (>500 µm) and micro-phenocrysts (100-500 µm) and microlites (<100 µm) in the groundmass.

Figures captions

Figure 1. A) SiO_2 composition versus duration, and B) Volume versus magma eruptive rates plotted for the Chachani Volcano Cluster and other clusters, compared to compound volcanoes (massifs) and individual composite volcanoes in CVZ, and other volcanic clusters worldwide. CVZ individual composite cones and compound volcanoes (red triangles) include: San Pedro (O'Callaghan and Francis, 1986), Ollagüe (Feeley et al., 1993; Feeley and Davidson, 1994), Lascar (Mathews et al., 1994), Llullaillaco (Richards and Villeneuve, 2011), El Misti (Thouret et al., 2001), Ubinas (Thouret et al., 2005), Tancitaro (Ownby et al., 2007), Parinacota (Hora et al., 2007), Auncanquilcha (Klemetti and Grunder, 2007), Uturuncu (Sparks et al., 2008; Muir et al., 2015) and Ampato-Sabancaya (Samaniego et al., 2016). Large volcano clusters, fields or complexes (blue triangles) encompass: Pichincha massif (Robin et al., 2010; Samaniego et al., 2010), Unzen (Hoshizumi et al., 1999), Taápaca (Clavero et al., 2004), and Coropuna cluster (Mariño et al., 2020). And for the purpose of comparison although the crust thickness is thinner than CVZ crust: Mt. Baker field (Hildreth et al., 2003), Mt. Adams field (Hildreth and Lanphere, 1994), and Mt. Mazama field (Bacon and Lanphere, 2006). Average eruptive rate has been calculated using bulk volume of erupted material for each of the volcanic systems. Two black dots with associated error range indicate the C-LVC maximum and minimum volume estimates.

Figure 2. Topographic map illustrating the location of the Chachani volcano complex and the regional geodynamic setting. AOH: Andagua-Orcopampa-Huambo monogenetic field; CLF: Chivay Lava Field. Subduction zone and convergence rate between Nazca and South American plates are indicated. Continuous and dashed lines delineate the extent of the Pleistocene-Holocene Frontal arc and the Early Quaternary volcano range, respectively. The map also

shows the monogenetic field of Andahua-Orcopampa-Huambo, and the principal rivers and cities or towns. Relief of image taken from Arc Map World Imagery Service. Topography and bathymetry data are from the SRTM15_PLUS version 1.0 data set.

Figure 3. Geological and structural map of the C-LVC in the Arequipa area. **A**. The morphotectonic scheme indicates two domains defined by Carlotto et al. (2009), combined with volcano-structural features (after Aguilar, 2015). Lithological data was taken from GEOCATMIN, INGEMMET (2014). **B**. Copernicus Sentinel-2 satellite image showing volcanic edifices composing the C-LVC. **C**. Sketch diagram showing how we interpret the transpressional tectonic setting in which the C-LVC has grown. Intersections (displayed in grey) of normal faults N80° that offset the strike-slip N130° faults together with Riedel N10° and 40° may act as preferential paths for C-LVC magmas. Graphic scale indicates that the diagram has been depicted at the scale of the map 3B.

Figure 4. Generalized map on DEM showing two, Old- and Young Edifice groups totaling twelve edifices forming the C-LVC and Pre-Chachani rocks. Red spots indicate the location of samples used for chemical analysis. Black dots indicate location of samples with $^{40}Ar/^{39}Ar$ (black text with white frame) and U/Pb (white text with black frame) ages expressed in ka. The initiation and end of both geological cross sections NNE-SSW and NNW-SSE (Fig. 5) are shown. Generalized stratigraphic section of the C-LVC (right-hand side).

Figure 5. Schematic geological sections showing the postulated structures and bedrock surface underneath the C-LVC. **A**. Cross section from the old Nocarane volcano (NNW) to the Cabreria dome (SSE) through the youngest Nevado Chachani cone. **B**. Cross section from Nocarane (NNE) to the Airport-Potrero dome cluster through the La Horqueta cumulo-dome. These two profiles are located with white dots on figure 6.

Figure 6. 3-D diagrams showing how we reconstructed the 'pre-Chachani' palaeo-topography based on DEM and interpolation of coordinates and elevation dataset from the geological map using Surfer software (Fig. 4). White, dashed lines indicate both cross sections shown in Figure 5. The interval between the contours lines is 200 meters.

Figure 7. Observed textures in thin sections of the C-LVC lavas. Photomicrographs in plane-polarized light suggest features attributed to magma mixing processes in lavas, as seen in: (**A**) Light and brown colored groundmass in Volcancillo; (**B**) Microlithic and glassy groundmass in Estribo stratovolcano. Back Scattered Electron images (BSE) showing the typical textures observed in the C-LVC samples; (**C**) Spongy cellular texture "sieve" in plagioclase; (**D**)

Pervasive resorption in amphibole; (**E**) Breakdown texture in biotite with orthopyroxene recrystallization; (**F**) resorption and recrystallization in olivine.

Figure 8. Compositional diversity of magmas of C-LVC lavas in the diagram SiO_2 versus K_2O (data from this work and Mamani et al., 2010), after Peccerillo and Taylor (1976), compared with available datasets of Pleistocene-Holocene lavas and lava-domes of the Andean CVZ (Wörner et al., 2018; Mamani et al., 2010; grey dots).

Figure 9. Variations in magma compositions as a function of time for all edifices of the C-LVC. The vertical position of samples illustrates their relative stratigraphic positions based on $^{40}Ar/^{39}Ar$ ages. * Age of Yura Tuffs emplaced between Pre-Chachani and C-LVC edifices.

Figure 10. Multi-element diagrams normalized to primitive mantle (Sun and McDonough, 1989) showing trace element patterns of the C-LVC lava samples. **A**. Old Edifice group, **B**. Young Edifice group. The grey backgrounds show the available datasets of Pleistocene-Holocene lavas and lava-domes of the Andean CVZ (Wörner et al., 2018; Mamani et al., 2010).

Figure 11. Plots of major and trace element ratios for the C-LVC, and the La Joya Ignimbrite (LJI, *c.* 4.9 Ma) and Arequipa Airport Ignimbrite (AAI, *c.* 1.62-1.66 Ma) for the purpose of comparison with post-caldera C-LVC magmas. Major elements for C-LVC, LJI and AAI show a similar pattern using silica content. Trace element (Ba, Th and Dy/Yb ratios) allow us to correlate AAI and C-LVC magmas and distinguish those from the LJI magma.

Figure 12. Variations in trace element signatures versus silica content observed in the C-LVC lavas compared to Pleistocene-Holocene lavas and lava domes in the Central Andes. (**A**) Ba/Sr plotted with respect to wt.% SiO_2. (**B**) Sr/Y plotted with respect to wt.% SiO_2. (**C**) Dy/Yb plotted with respect to wt.% SiO_2. (**D**) Sm/Yb plotted with respect to wt.% SiO_2. Arrows indicate compositional variations caused by the distinct preference for certain trace elements in the different residual mineral phases during fractional crystallization and/or crustal melting and assimilation. Abbreviations are as follows: cpx= clinopyroxene; plag= plagioclase feldspar. Grey dots represent the available dataset for the frontal arc of CVZ (Wörner et al., 2018; Mamani et al., 2010).

Figure 13. Plots of Ni versus Rb for lavas from C-LVC. The plots show a scattered negative correlation of compatible elements (Ni) with incompatible element (Rb) suggest an important role of magma mixing in the C-LVC evolution.

Figure 14. A) Diagram FeO (wt. %) vs An (anorthite), displaying variations of plagioclase and their trend suggesting the influence of magma mixing/mingling. The plots show small variation of FeO and anorthite for phenocrysts. On the other hand, microlites and crystal rims show considerable variations indicating hotter, less dense recharge in the magma chamber and/or heating event prior to the eruptive event. **B)** Mg# versus ^{IV}AL and **C)** ^{IV}Al versus total displaying variation of amphibole composition.

Figure 15. Trace element signatures in the C-LVC lavas for the purpose of comparison with available datasets of the Andean CVZ magmas (Wörner et al., 2018; Mamani et al., 2010; grey dots and grey background). **(A)** Sr/Y ratios plotted with respect to wt.% SiO_2. **(B)** Ratios of Dy/Yb plotted with respect to wt.% SiO_2. **(C)** Dy/Yb ratios plotted with respect to Sm/Yb. **(D)** Ratio of Sm/Yb plotted with respect to stratigraphic position; the gray box represents the range of Sm/Yb ratio of Quaternary lavas in the Central Andes. Overall, C-LVC lavas fall into intermediate values compared to the analyzed Andean CVZ magmas of Quaternary age.

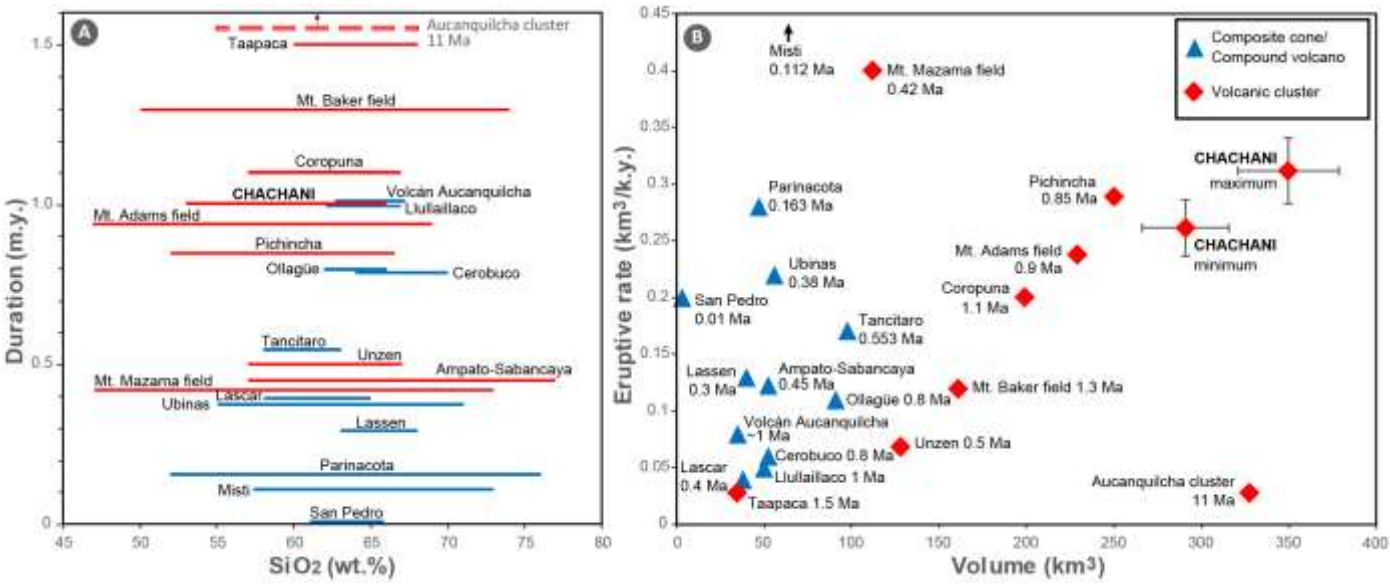

Figure 1. A) SiO_2 composition versus duration, and B) Volume versus magma eruptive rates plotted for the Chachani Volcano Cluster and other clusters, compared to compound volcanoes (massifs) and individual composite volcanoes in CVZ, and other volcanic clusters worldwide. CVZ individual composite cones and compound volcanoes (red triangles) include: San Pedro (O'Callaghan and Francis, 1986), Ollagüe (Feeley et al., 1993; Feeley and Davidson, 1994), Lascar (Matthews et al., 1994), Llullaillaco (Richards and Villeneuve, 2011), El Misti (Thouret et al., 2001), Ubinas (Thouret et al., 2005), Tancitaro (Ownby et al., 2007), Parinacota (Hora et al., 2007), Auncanquilcha (Klemetti and Grunder, 2007), Uturuncu (Sparks et al., 2008; Muir et al., 2015) and Ampato-Sabancaya (Samaniego et al., 2016). Large volcano clusters, fields or complexes (blue triangles) encompass: Pichincha massif (Robin et al., 2007; Samaniego et al., 2010), Unzen (Hoshizumi et al., 1999), Taápaca (Clavero et al., 2004), and Coropuna cluster (Mariño et al., 2020). And for the purpose of comparison although the crust thickness is thinner than CVZ crust: Mt. Baker field (Hildreth et al., 2003), Mt. Adams field (Hildreth and Lanphere, 1994), and Mt. Mazama field (Bacon and Lanphere, 2006). Average eruptive rate has been calculated using bulk volume of erupted material for each of the volcanic systems. Two black dots with associated error range indicate the C-LVC maximum and minimum volume estimates.

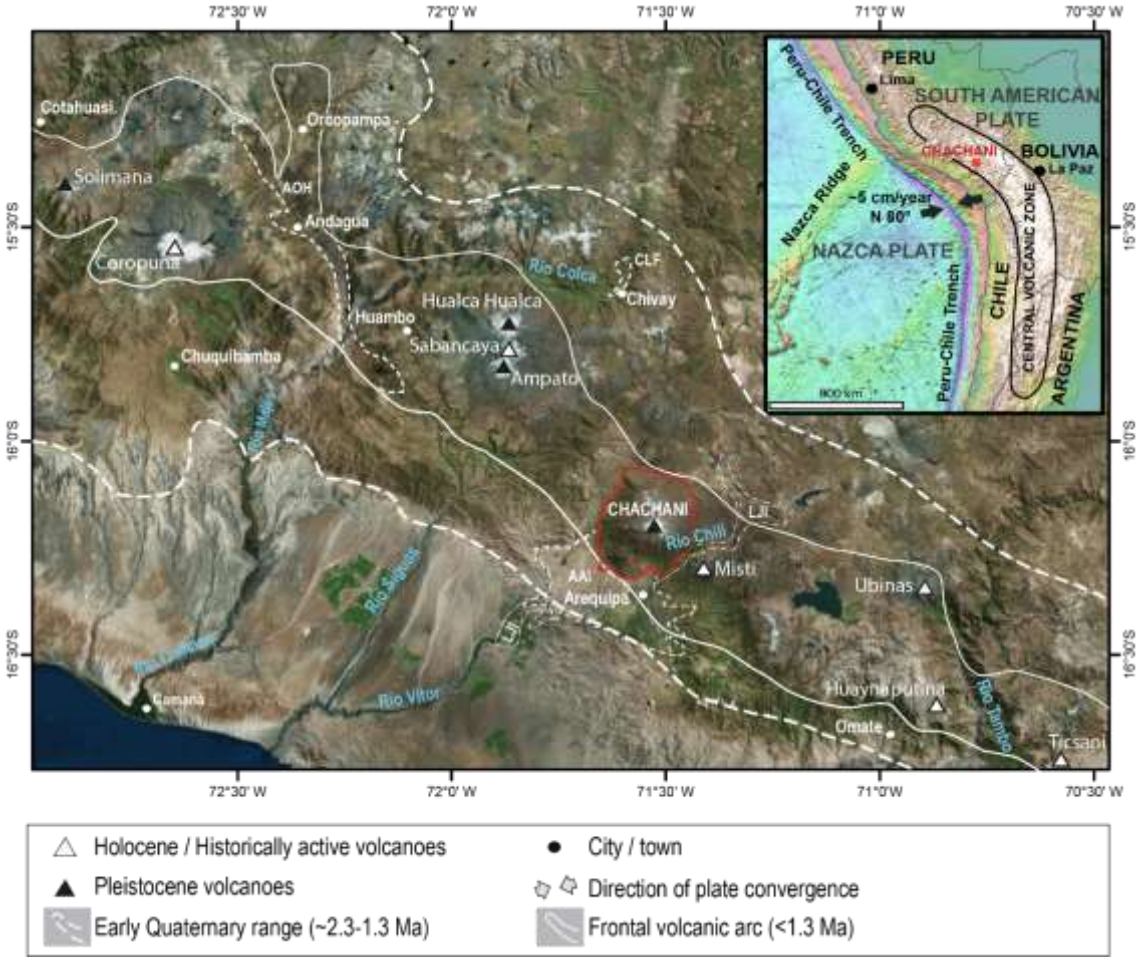

Figure 2. Topographic map illustrating the location of the Chachani volcano complex and the regional geodynamic setting. AOH: Andagua-Orcopampa-Huambo monogenetic field; CLF: Chivay Lava Field. Subduction zone and convergence rate between Nazca and South American plates are indicated. Continuous and dashed lines delineate the extent of the Pleistocene-Holocene Frontal arc and the Early Quaternary volcano range, respectively. The map also shows the monogenetic field of Andahua-Orcopampa-Huambo, and the principal rivers and cities or towns. Relief of image taken from Arc Map World Imagery Service. Topography and bathymetry data are from the SRTM15_PLUS version 1.0 data set.

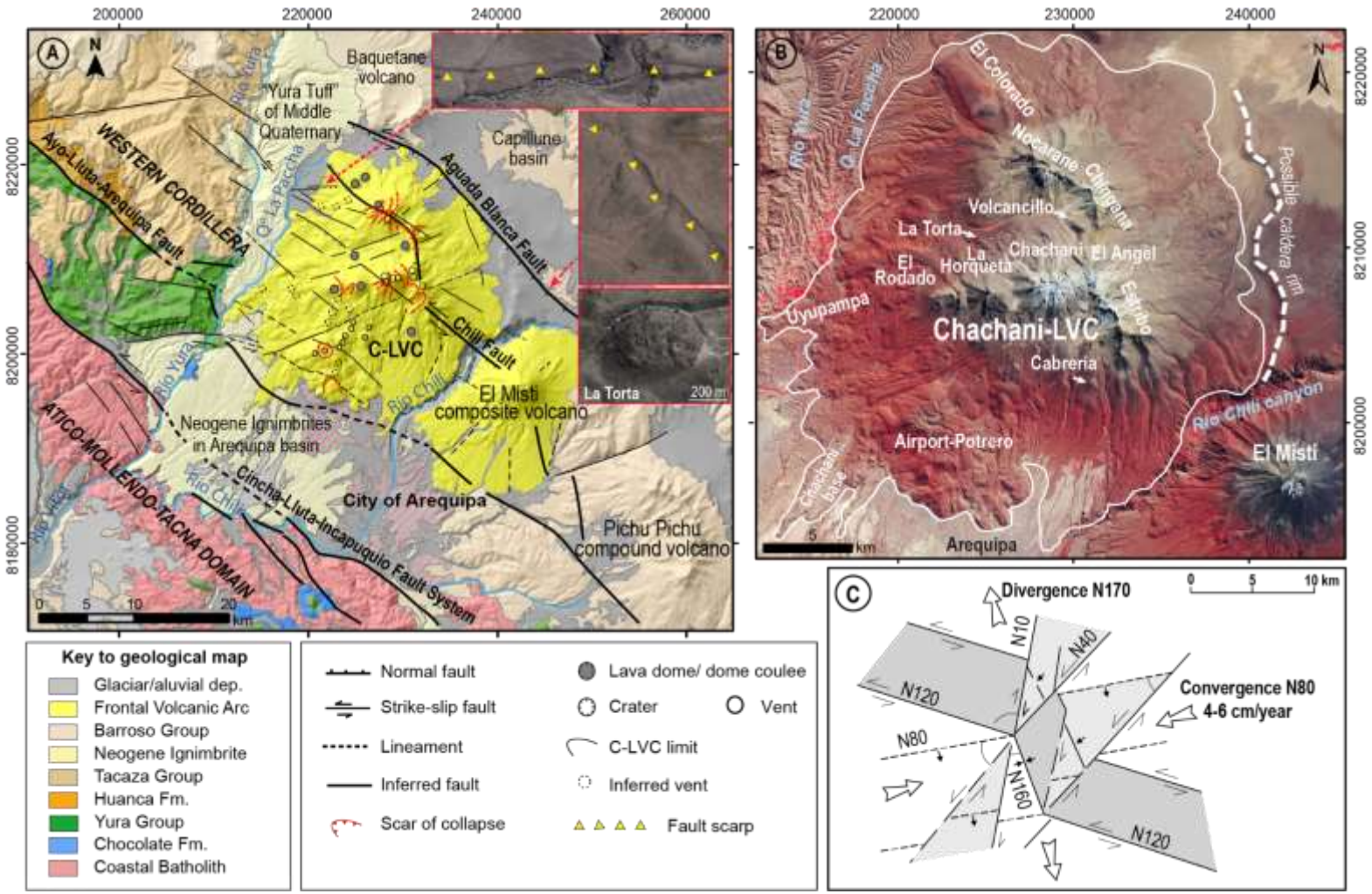

Figure 3. Geological and structural map of the C-LVC in the Arequipa area. **A**. The morphotectonic scheme indicates two domains defined by Carlotto et al. (2009), combined with volcano-structural features (after Aguilar, 2015). Lithological data was taken from GEOCATMIN, INGEMMET (2014). **B**. Satellite image showing volcanic edifices composing the C-LVC. The **C**. Sketch diagram showing how we interpret the transpressional tectonic setting in which the C-LVC has grown. Intersections (displayed in grey) of normal faults N80° that offset the strike-slip N130° faults together with Riedel N10° and 40° may act as preferential paths for C-LVC magmas. Graphic scale indicates that the diagram has been depicted at the scale of the map 3B.

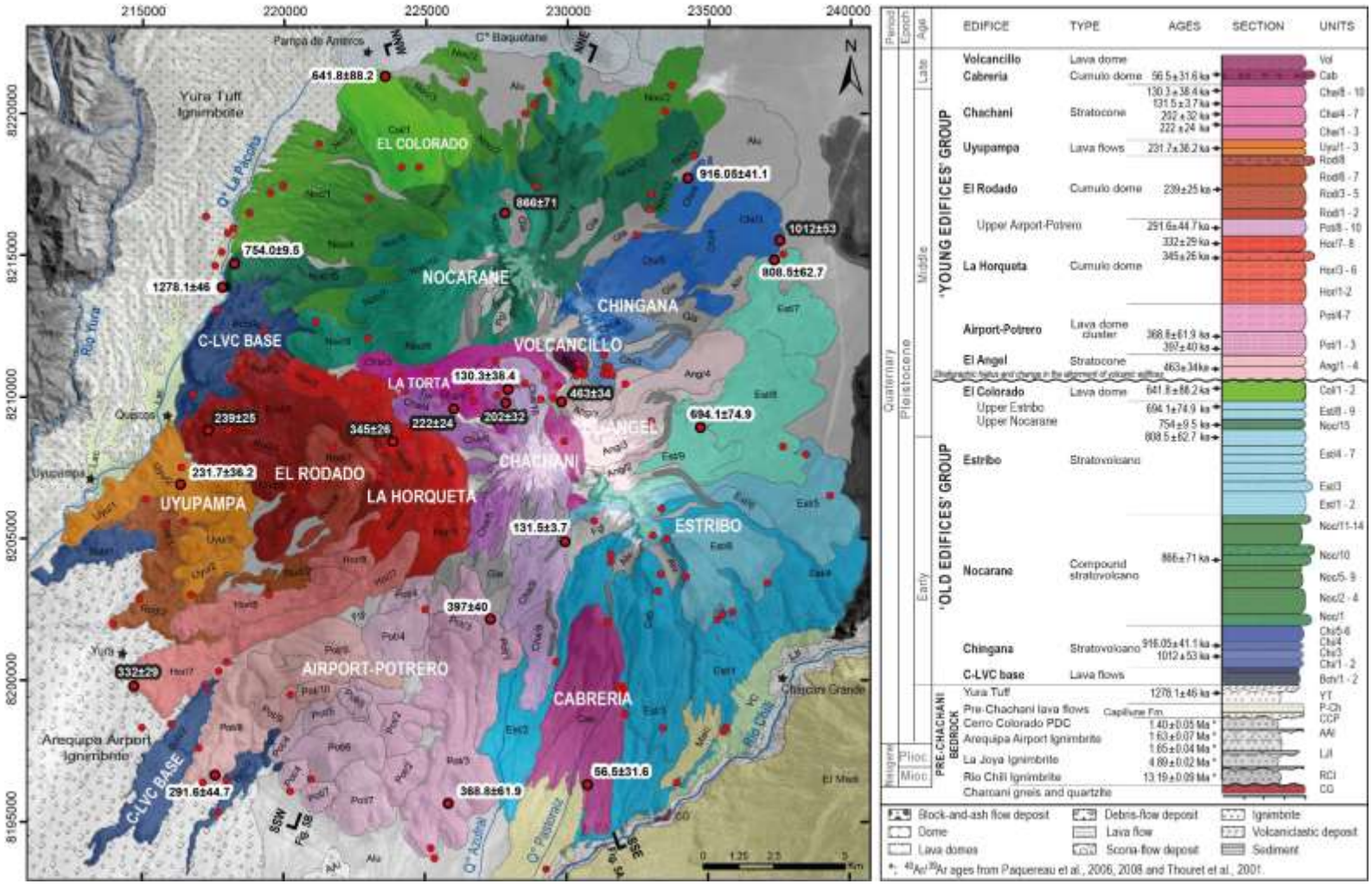

Figure 4. Generalized map on DEM showing two, 'Old-' and 'Young edifices' groups totaling twelve edifices forming the C-LVC and Pre-Chachani rocks. Red spots indicate the location of samples used for chemical analysis. Black dots indicate location of samples with $^{40}Ar/^{39}Ar$ (black text with white frame) and U/Pb (white text with black frame) ages expressed in ka. The initiation and end of both geological cross sections NNE-SSW and NNW-SSE (Fig. 5) are shown. Generalized stratigraphic section of the C-LVC (right).

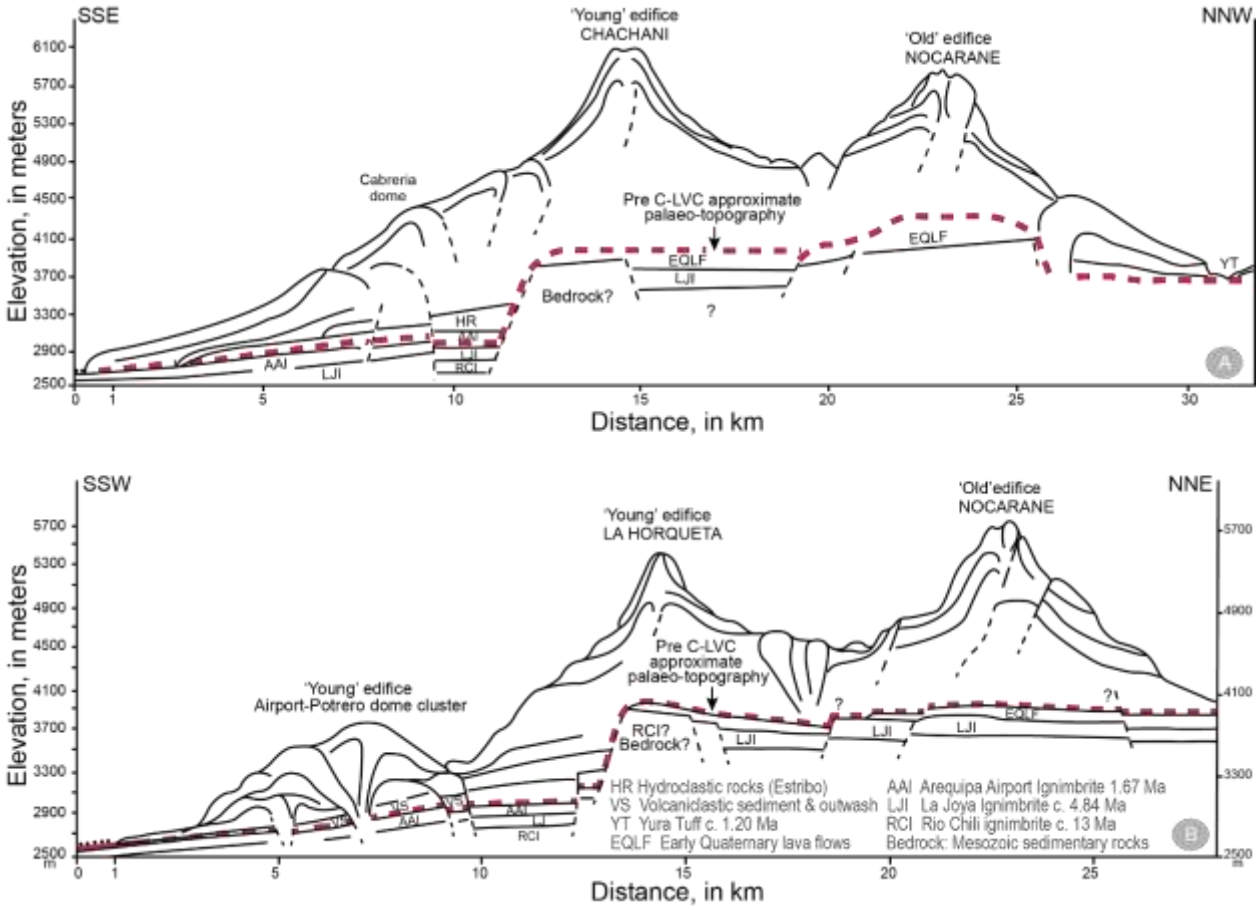

Figure 5. Schematic geological sections showing the postulated structures and bedrock surface underneath the C-LVC. **A**. Cross section from the old Nocarane volcano (NNW) to the 'young' Cabreria dome (SSE) through the youngest Nevado Chachani cone. **B**. Cross section from Nocarane (NNE) to the 'young' Airport dome cluster through the 'young' La Horqueta cumulo-dome. These two profiles are located with white dots on figure 6.

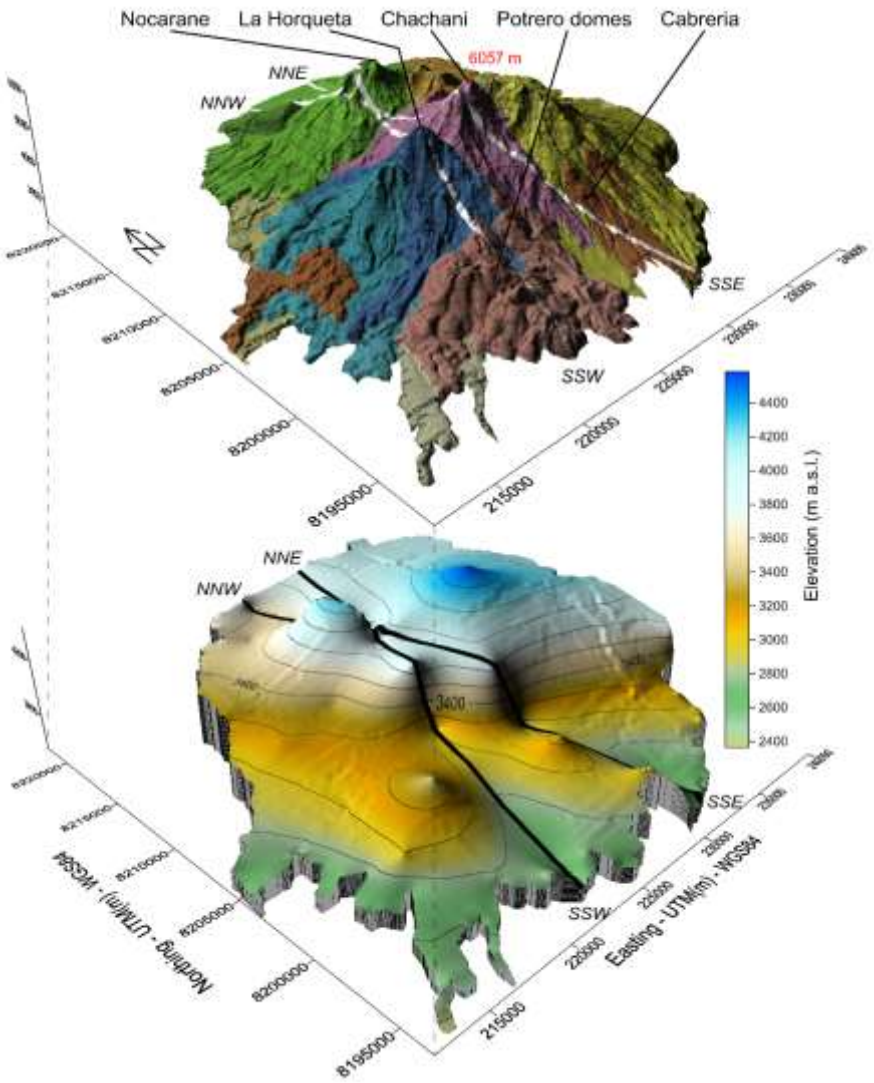

Figure 6. 3-D diagrams showing how we reconstructed the pre-Chachani palaeo-topography based on DEM and interpolation of coordinates and elevation dataset from the geological map using Surfer software (Fig. 4). White or black bold lines indicate both cross sections shown in Figure 5. The interval between the contours lines is 200 meters. Colors code on the geological map: same as figure 4.

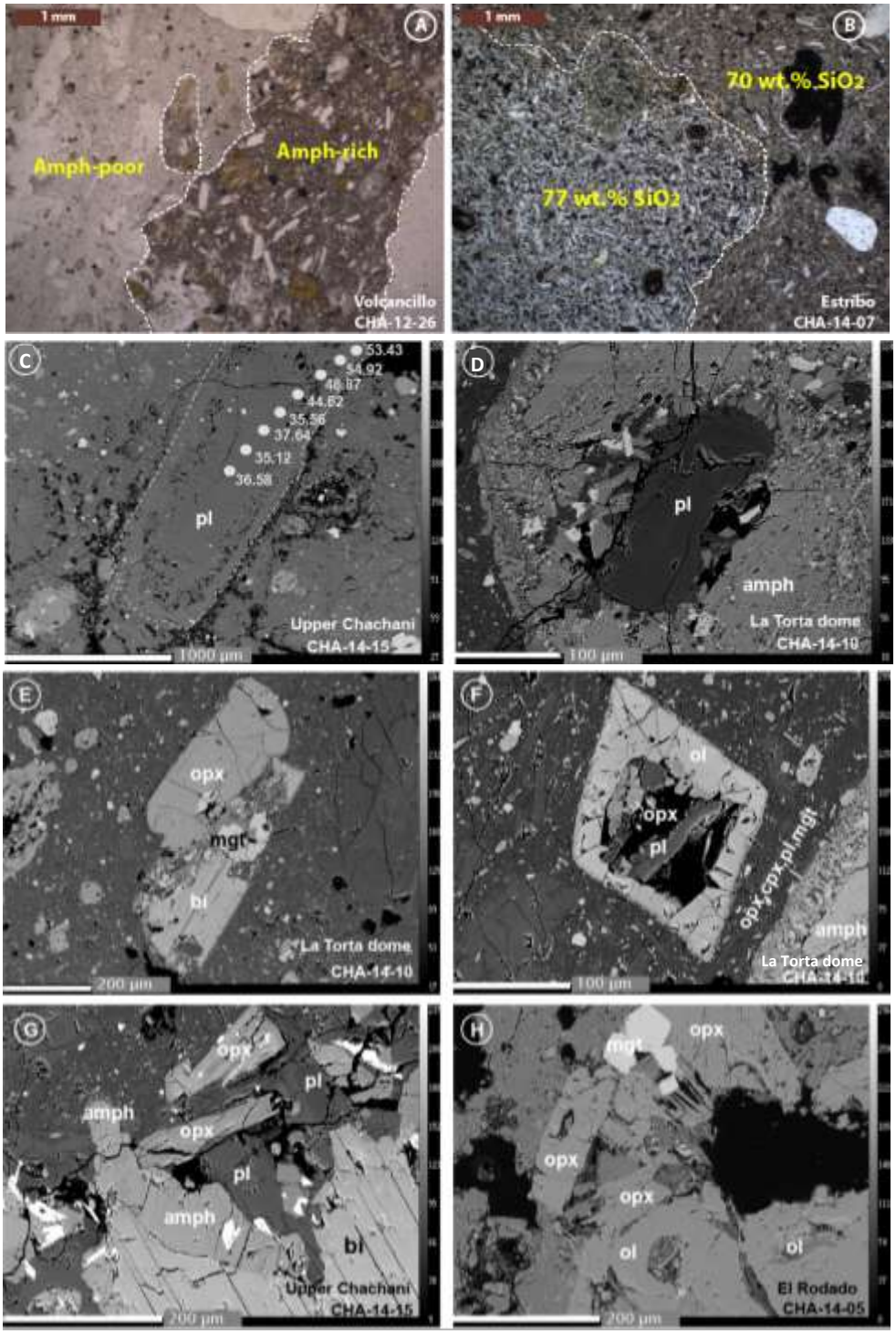

Figure 7. Observed textures in thin sections of the C-LVC lavas. Photomicrographs in plane-polarized light suggest features attributed to magma mixing processes in lavas, as seen in: (**A**) Light and brown colored groundmass in Volcancillo; (**B**) Microlithic and glassy groundmass in Estribo stratovolcano. Back Scattered Electron images (BSE) showing the typical textures observed in the C-LVC samples; (**C**) Spongy cellular texture "sieve" in plagioclase; (**D**) Pervasive resorption in amphibole; (**E**) Breakdown texture in biotite with orthopyroxene recrystallization; (**F**) resorption and recrystallization in olivine

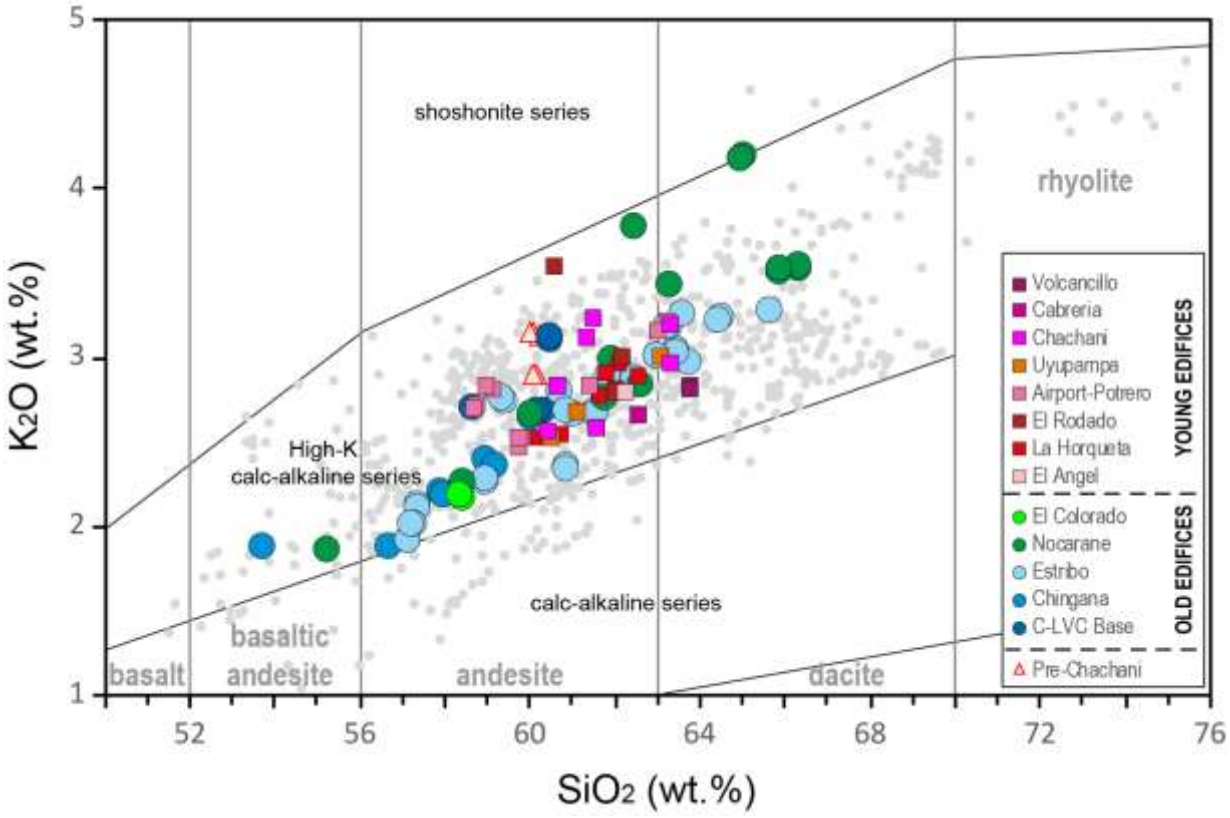

Figure 8. Compositional diversity of magmas of C-LVC lavas in the diagram SiO_2 versus K_2O (data from this work and Mamani et al., 2010), after Peccerillo and Taylor (1976), compared with available datasets of Pleistocene-Holocene lavas and lava-domes of the Andean CVZ (Wörner et al., 2018; Mamani et al., 2010; grey dots).

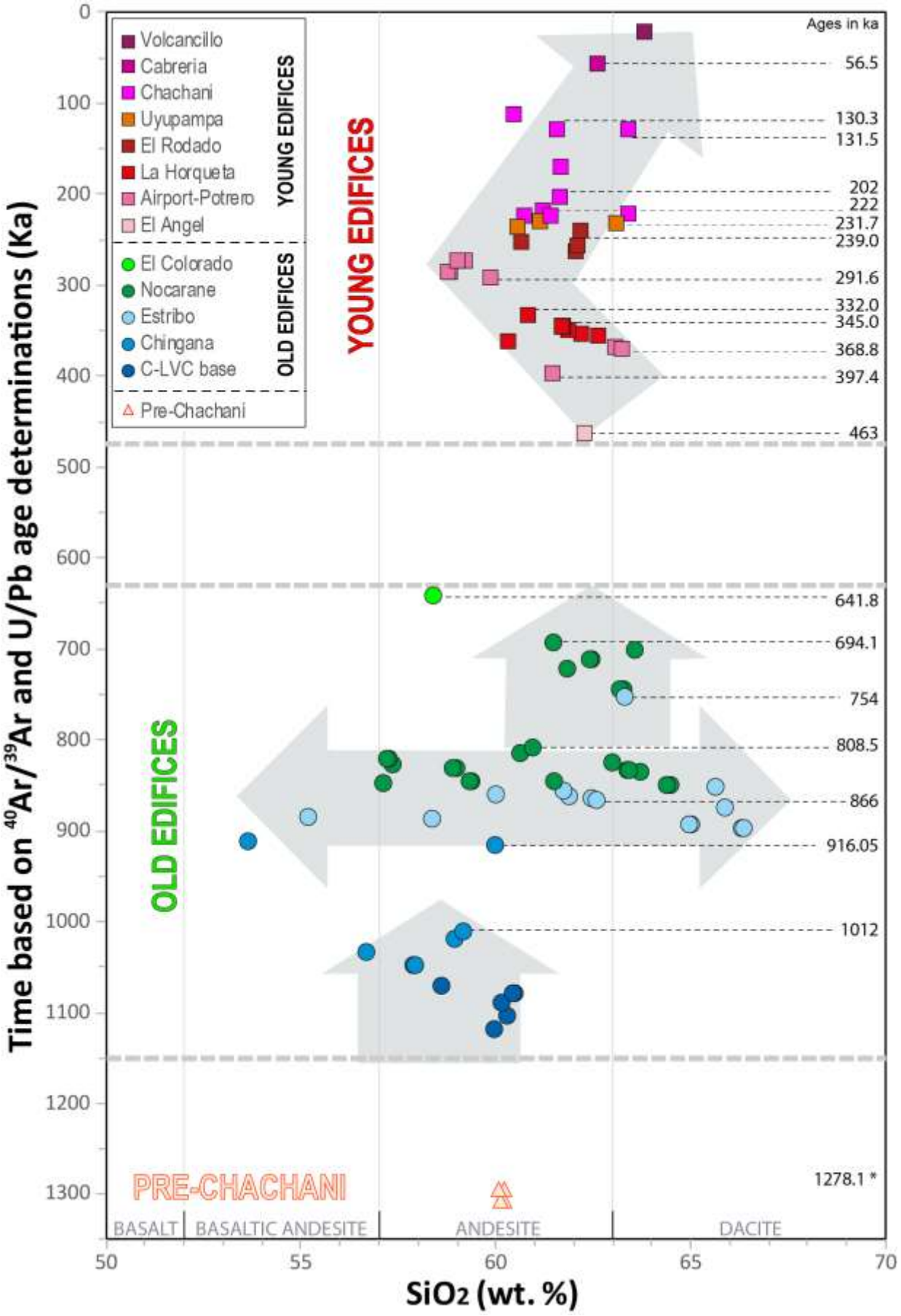

Figure 9. Variations in magma compositions as a function of time for all edifices of the C-LVC. The vertical position of samples illustrates their relative stratigraphic positions based on $^{40}Ar/^{39}Ar$ ages. * Age of Yura Tuffs emplaced between Pre-Chachani and C-LVC edifices.

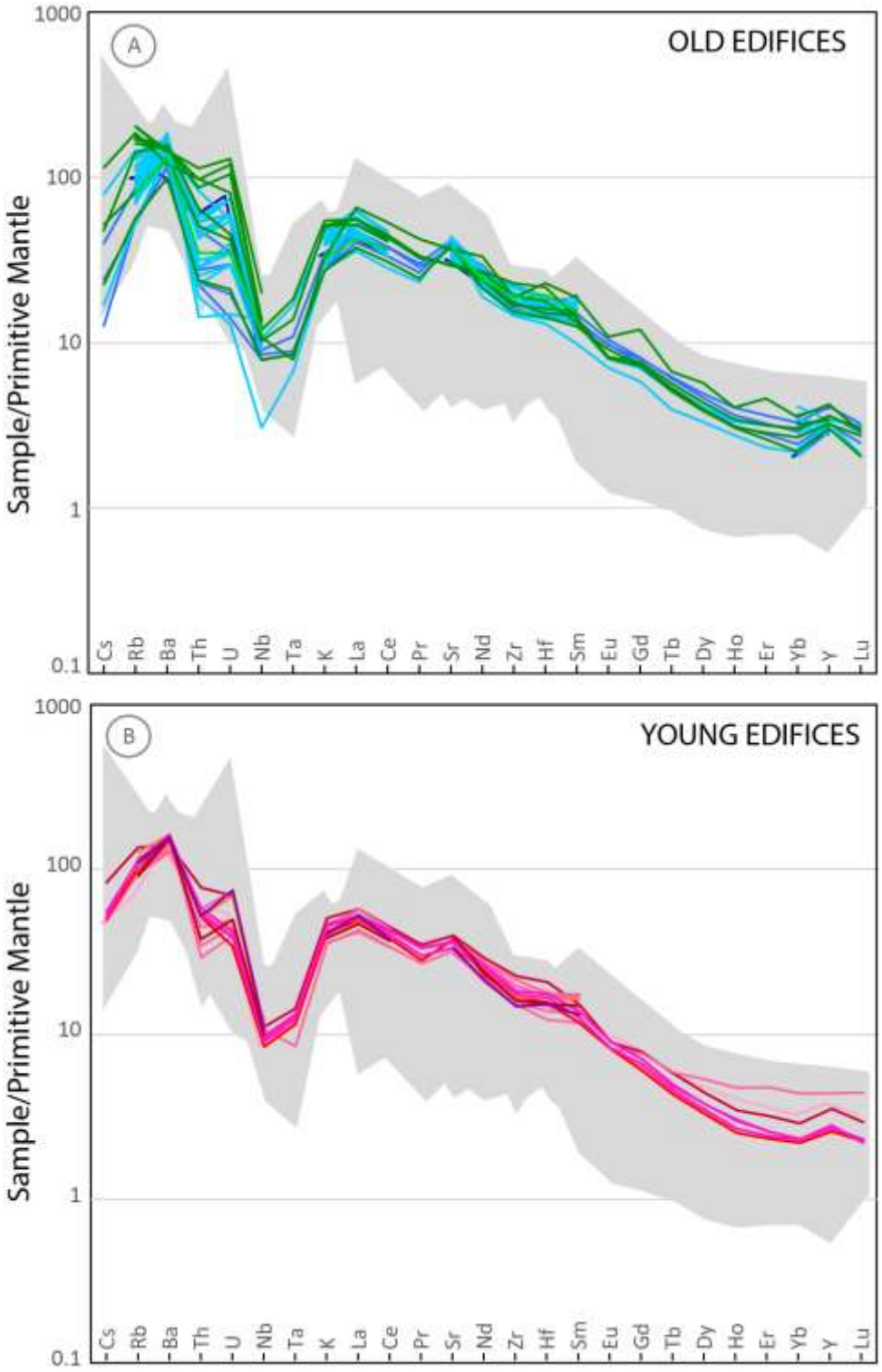

Figure 10. Multi-element diagrams normalized to primitive mantle (Sun and McDonough, 1989) showing trace element patterns of the C-LVC lava samples. **A**. 'Old' edifices, **B**. 'Young' edifices. The grey backgrounds show the available datasets of Pleistocene-Holocene lavas and lava-domes of the Andean CVZ (Wörner et al., 2018; Mamani et al., 2010).

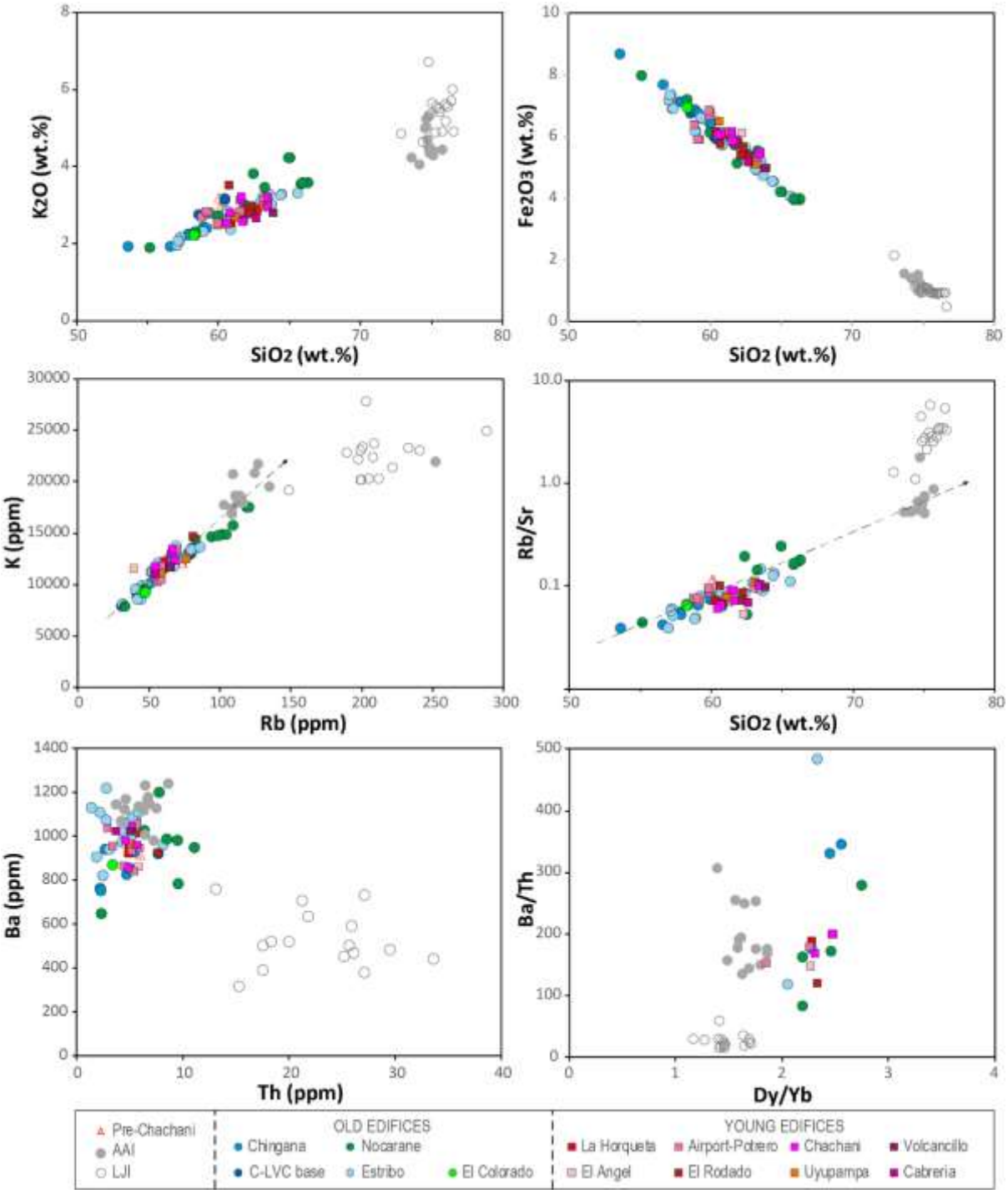

Figure 11. Plots of major and trace element ratios for the C-LVC, and the La Joya Ignimbrite (LJI, c.4.9 Ma) and Arequipa Airport Ignimbrite (AAI, c.1.62-1.66 Ma) for the purpose of comparison with post-caldera C-LVC magmas. Major elements for C-LVC, LJI and AAI show a similar pattern using silica content. Trace element (Ba, Th and Dy/Yb ratios) allow us to correlate AAI and C-LVC magmas and distinguish those from the LJI magma.

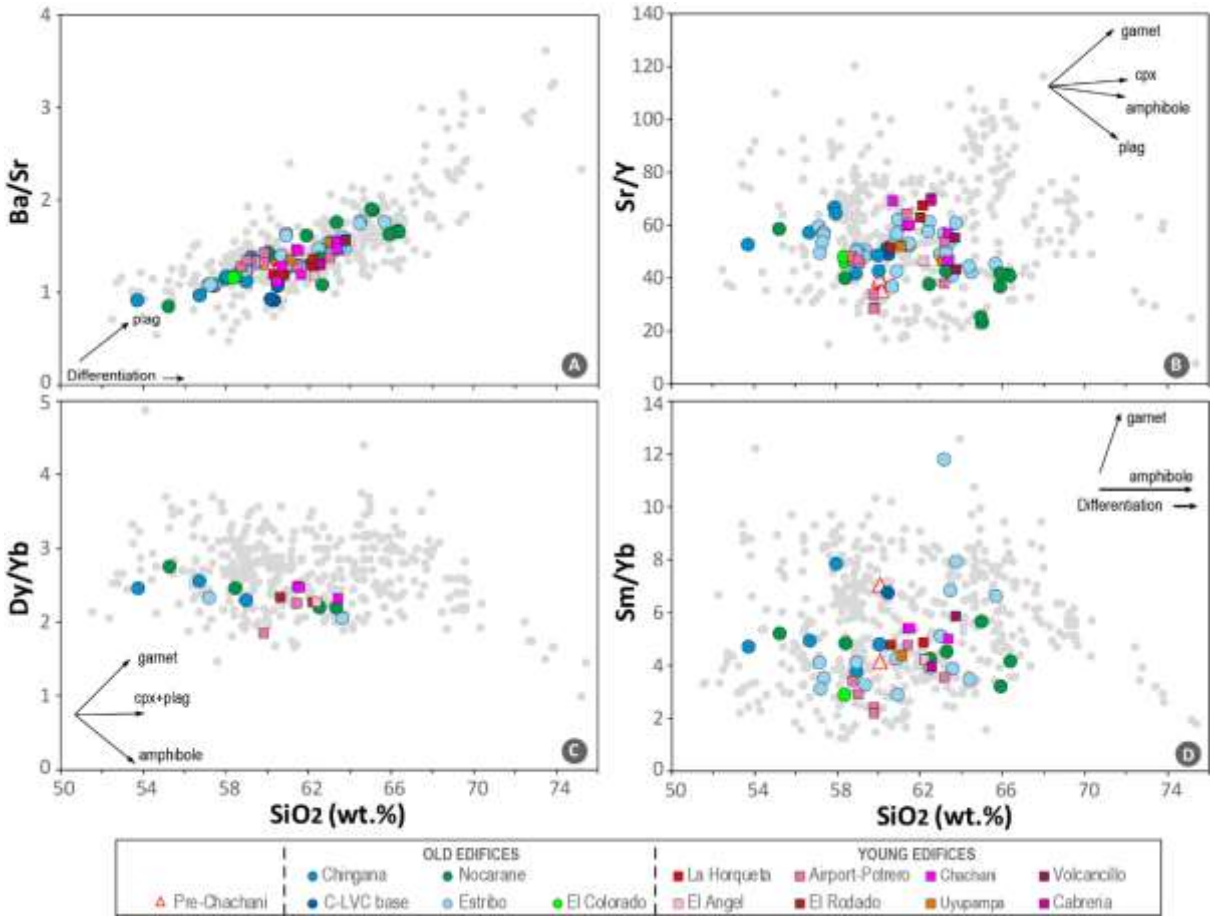

Figure 12. Variations in trace element signatures versus silica content observed in the C-LVC lavas compared to Pleistocene-Holocene lavas and lava domes in the Central Andes. (**A**) Ba/Sr plotted with respect to wt% SiO_2. (**B**) Sr/Y plotted with respect to wt% SiO_2. (**C**) Dy/Yb plotted with respect to wt% SiO_2. (**D**) Sm/Yb plotted with respect to wt% SiO_2. Arrows indicate compositional variations caused by the distinct preference for certain trace elements in the different residual mineral phases during fractional crystallization and/or crustal melting and assimilation. Abbreviations are as follows: cpx= clinopyroxene; plag= plagioclase feldspar. Grey dots represent the available dataset for the frontal arc of CVZ (Wörner et al., 2018; Mamani et al., 2010).

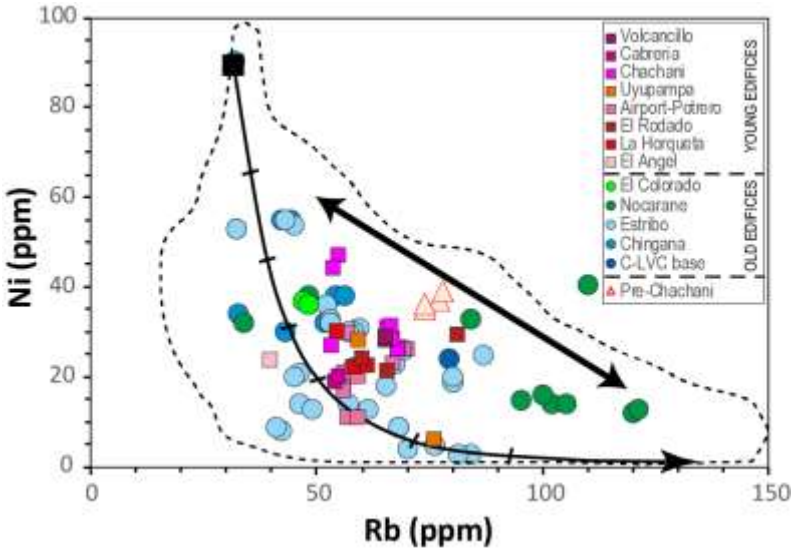

Figure 13. Plots of Ni versus Rb for lavas from C-LVC. The plots show a scattered negative correlation of compatible elements (Ni) with incompatible element (Rb) suggest an important role of magma mixing in the C-LVC evolution.

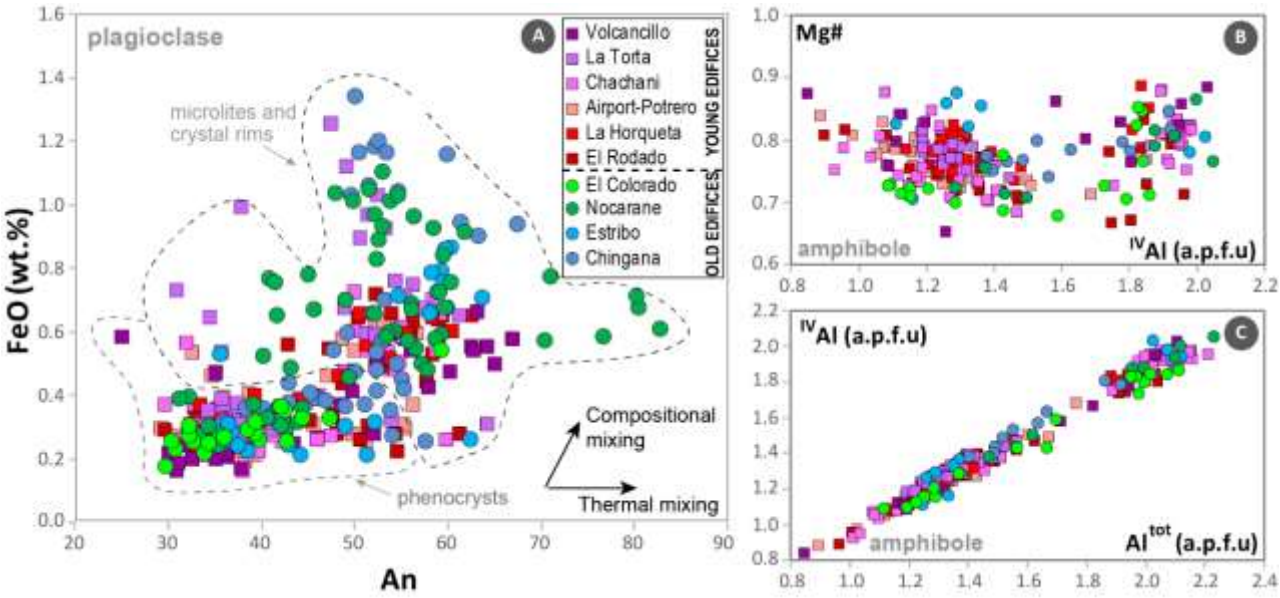

Figure 14. A) Diagram FeO (wt. %) vs An (anorthite), displaying variations of plagioclase and their trend suggesting the influence of magma mixing/mingling. The plots show small variation of FeO and anorthite for phenocrysts. On the other hand, microlites and crystal rims show considerable variations indicating hotter, less dense recharge in the magma chamber and/or heating event prior to the eruptive event. **B)** Mg# versus ^{IV}AL and **C)** ^{IV}Al versus total displaying variation of amphibole composition.

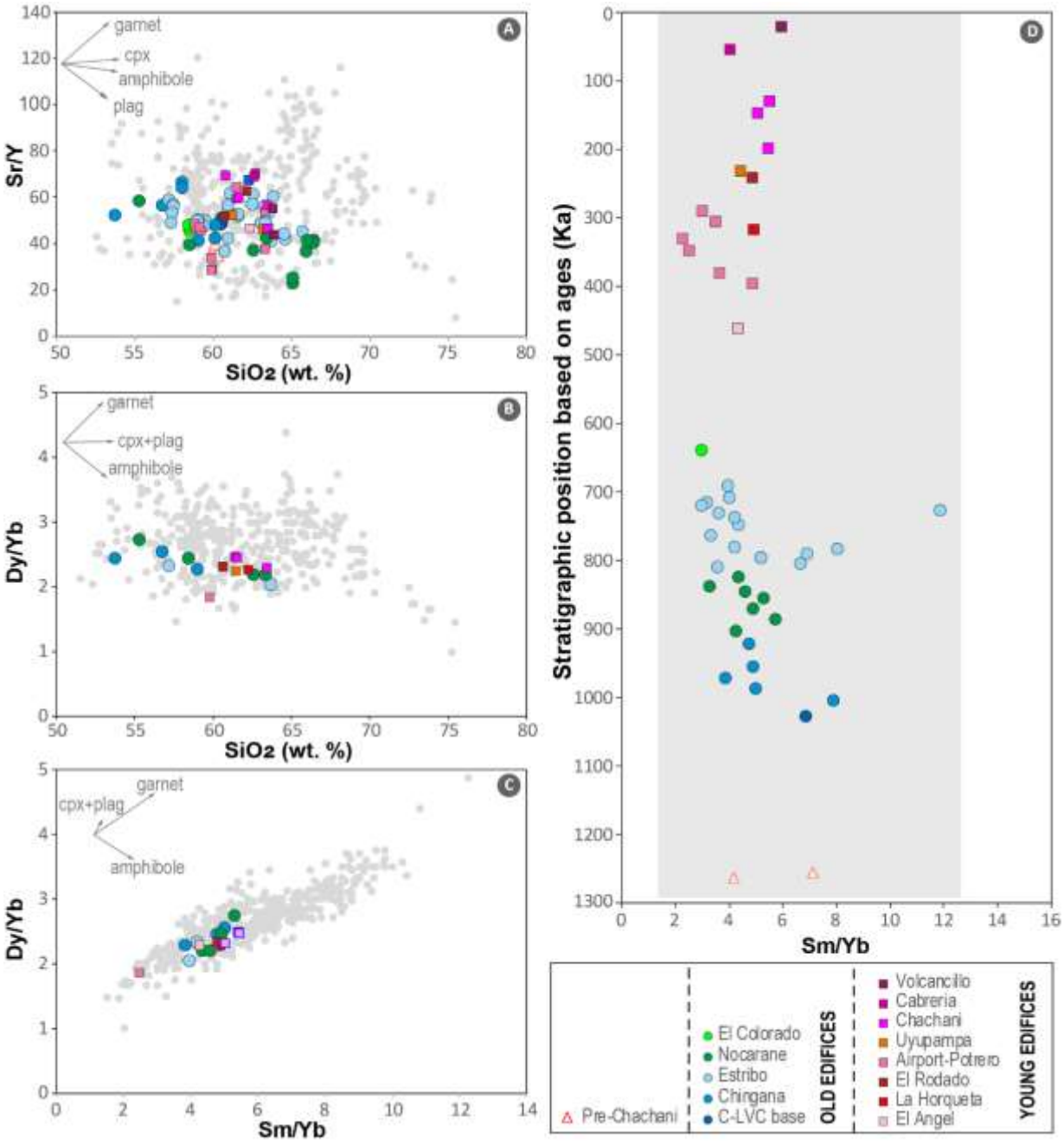

Figure 15. Trace element signatures in the C-LVC lavas for the purpose of comparison with available datasets of the Andean CVZ magmas (Wörner et al., 2018; Mamani et al., 2010; grey dots and grey background). **(A)** Sr/Y ratios plotted with respect to w% SiO_2. **(B)** Ratios of Dy/Yb plotted with respect to w% SiO_2. **(C)** Dy/Yb ratios plotted with respect to Sm/Yb. **(D)** Ratio of Sm/Yb plotted with respect to stratigraphic position; the gray box represents the range of Sm/Yb ratio of Quaternary lavas in the Central Andes. Overall, C-LVC lavas fall into intermediate values compared to the analyzed Andean CVZ magmas of Quaternary age.

Large volcanic cluster, LVC. Compound volcano (massif)	**Surface** (km^2)	**Volume** (km^3) ± 10%	**No. of erup tive centres**	**Lifetime** (Ma)	**Eruptive pulses / stages** Ma	**DRE magma production** km^3	**Bulk magma output rate** km^3/kyr	**Compositional range**	**Caldera**: associated or buried	**Reference**
Chachani LVC, CVZ, S Peru	580-600	Min c. 290 Max 350 ± 29/35	12	1.27	2: 'old' 1.1-0.6, 'young' 0.4-0.05	198–231 (80% lava flows)	Aver. 0.14-0.22 Peak 0.28-0.3 'Old' group: 'Young' group:	Mafic andesite to dacite	Probably buried	This study: geologic map & DEM Figs. 4, 6: Cross sections Fig. 5
Coropuna LVC, CVZ, S Peru	400-450	135-200	5	1.1	4: 'old' 1.1-0.4, 'young' 0.2-0.0014	130-180 (90% lava flows)	Aver. 0.2 Peak 0.3	Mafic andesite to dacite	Probably buried	Mariño et al., 2020
Ampato (A) – Sabancaya (S) massif, CVZ, S Peru	c. 240-260	A 38-42 S 6-10 Total 44-54	3 1	A 0.4-0.45 S 0.005-0.01	5 Ampato 0.45-0.1 1 Sabancaya 0.01-0.005	40-50	A 0.10-0.12 S 0.6-1.7 (max) Aver. 0.08-0.09	Andesite and dacite	Probably buried?	Samaniego et al., 2016; Thouret et al., 1994; Bromley et al., 2019
Aucanquilcha massif, CVZ, N Chile	c. 80	37	1	1	4	70	Av. 0.04 – 0.10 Peak 0.16	Dacite		Klemetti and Grunder, 2007
Aucanquilcha Cluster, CVZ, N Chile	700	327 ± 20	19	11	3 (1.5 to 3 Myr)	300	Av. 0.03 Peak 0.11-0.22	Mafic andesite to dacite		Grunder et al., 2008; Walker et al, 2013
Lastarria - Cordón del Azufre LVC, CVZ Chile -Argentina	LVC 500 Lastarria 90	45 Lastarria 200 cluster	7	0.6 – <0.3	4 Lastarria 3 Cordón del Azufre	40 180	0.1-0.15 Max 0.33	Andesite and dacite	Yes Current inflation	Naranjo, 1992; Froger et al., 2007
Payachata Parinacota stratovolcanoes, CVZ, N Chile	190 50	Parinacota 46 Pomerape 40	2	0.163	4 Parinacota	40 35	Parinacota 0.25-0.31 (max 0.5-1.2)	Dacite and rhyolite		Wörner et al., 1988; Davidson et al., 1990; Hora et al., 2007
Ollagüe compound volcano, CVZ, N Chile	480	80-90	>7	< 1	4	70-80	Aver. 0.07-0.08	dacite		Feeley & Davidson, 1994
Llullaillaco compound volcano, CVZ, N Chile	150	50-60	4	1.5 – 0.048	2	40-50	Aver. 0.04-0.06	dacite		Richards and Villeneuve, 2001
Taapaca compound volcano, CVZ, N Chile	180-250	35 - 73	4	1.5	4	30-65	0.05 domes; 0.07 comp. volc.	dacite		Clavero et al., 2004
Lascar stratovolcano, CVZ, N Chile	55-185	50-60	3	< 0.43	4	30–40	Aver. 0.02-0.03 Peak 0.14	dacite		Gardeweg et al., 1998 Mathews et al., 1994
For the purpose of comparison										

Mt. Mazama and volcanic field, Cascades, USA	500	58-112	many	0.42	many	100-120	0.42 Peak 0.8 Volc Field 0.07	Mafic andesite to rhyodacite	Crater Lake caldera	Bacon and Lanphere, 2006
Mt. Adams and volcanic field, Cascades, USA	1250	230-400	Many	0.94	many		Aver. 0.24-0.42	Basalt to dacite		Hildreth and Lanphere, 1994
El Misti individual composite cone	105-130	70-83	2	<0.835max <0.112min	4	55-65	Aver. 0.63 Peak 2.1	Andesite to rhyolite	Summit caldera	Thouret et al., 2001 Rivera et al., 2017
Ubinas individual composite cone	65 - 90	55-60	1	0.376 - Present	2	45-55	Aver. 0.17-0.22	Mafic andesite to rhyolite	Summit caldera	Thouret et al., 2005 Rivera et al., 2014
Andean stratocones		69 - 89		< 1 Ma						Karátson et al., 2012

Table 1. Characteristics of large volcanic clusters (LVCs) and comparison with compound volcanoes and individual composite stratocones in the Andean CVZ and elsewhere.

Sample	Edifice	Unit	UTM coordinates		Lithology	Material	Ages, ka ± 2σ [1] $^{40}Ar/^{39}Ar$ [2] U/Pb
			North	East			
'Young' edifice group							
CHA-02-32	Cabrería	Ca-1	8196348	230640	lava	groundmass	56.5 ± 31.6 [1]
CHA-12-26 CHA-08-44	Chachani	Cha10	8210279	227958	lava	groundmass	130.3 ± 38.4 [1]
CHA-08- 31	Chachani	Cha8	8204909	230078	lava	groundmass	131.5 ± 3.7 [1]
CHA-14-15	Chachani	Cha6	8209905	226802	lava	zircon	202 ± 32 [2]
CHA-14-17	Chachani	Cha4	8209523	226089	lava	zircon	222 ± 24 [2]
CHA-02-33	Uyupampa	Uyu-1	8206885	216438	lava	groundmass	231.7 ± 36.2 [1]
CHA-04-02	Potrero Domes	Dae-8	8196669	217651	lava	plagioclase	291.6 ± 44.7 [1]
CHA-14-05	El Rodado	Rod5	8208887	217435	lava	zircon	239 ± 25 [2]
CHA-14-02	La Horqueta	Hor7	8199845	214803	lava	zircon	332 ± 29 [2]
CHA-14-19	La Horqueta	Hor5	8208413	223942	lava	zircon	345 ± 26 [2]
CHA-02-04-JC	Potrero domes	Dae3	8195641	225903	lava	groundmass	368.8 ± 61.9 [1]
CHA-12-05	Potrero Domes	Dae1	8202150	227400	lava	groundmass	397 ± 40 [1]
CHA-12-24	El Angel	Ang1	8209865	229815	lava	zircon	463 ± 34 [2]
'Old' edifice group							
CHA-02-19	El Colorado	Col1	8221403	223762	lava	groundmass	641.8 ± 88.2 [1]
CHA-02-17	Estribo	Estr10	8208953	234803	lava	groundmass	694.1 ± 74.9 [1]
CHA-02-06-JC	Nocarane	Noc11	8199784	231938	lava	groundmass	754.0 ± 9.5 [1]
CHA-02-24	Estribo	Est8	8215060	237388	lava	plagioclase	808.5 ± 62.7 [1]
CHA-14-12	Nocarane	Noc10	8216424	227893	lava	zircon	866 ± 71 [2]
CHA-02-26	Chingana	Chi4	8217759	234368	lava	groundmass	916.5 ± 41.1 [1]
CHA-14-06	Chingana	Chi3	8215505	237644	lava	zircon	1012 ± 53 [2]
CHA-08-07*	Yura Tuff		8214022	217998	Pumice	Plagioclase	1278.1 ± 46 [1]

Table 2. $^{40}Ar/^{39}Ar$ and U/Pb ages of the large Chachani volcano cluster C-LVC and the neighbouring Yura tuffs. Chronology analytical data is presented in ESD Table 3.

Edifice	Age range (ka)	Estimated duration (ka)	Volume (km^3)	Eruptive rate (km^3/kyr)	Mineral assemblage	SiO_2 wt% range	K_2O (wt%) range
'Young' edifice group							
Volcancillo	? <150?	<50	0.33-0.39	0.006-0.007	Pl ± amp ± bi	63-65	2.5-2.7
Cabrería	56.5 - <130	50?	4.13-4.91	0.082-0.098	Pl ± amp	61-63	2.4-2.6
Chachani	130*-131.5	90-130	30.34-33.20	0.275-0.302	Pl ± opx ± amp ± (biot) Pl ± amp ± px	61-63	2.6-3.3
Uyupampa	231- ?	50-100?	2.36-2.72	0.031-0.036	Pl ± amp ± bi	61-63	2.8-3.0
El Rodado	>400 - <600	200	6.26-9.17	0.031-0.045	Pl ± cpx ± (ol)	60-62	2.5-3.6
La Horqueta	>400 - <600	200	3.24-6.46	0.032-0.064	Pl ± amp ± bi ± (cpx)	60-62	2.5-3.0
Potrero Domes	291 – 396	100	11.22-12.53	0.112-0.125	Pl ± amp ± cpx ± biot	58-63	2.5-3.5
El Angel	640? - 694	60-100	4.86-5.56	0.060-0.069	Pl ± amp ± cpx ± (biot)	61-63	2.7-2.9
'Old' edifice group							
El Colorado	640-642	<50	4.13-6.16	0.082 - 0.123	Pl ± amp ± bi	57-69	2.1-2.3
Estribo	694 - <916	220-250	59.35-63.03	0.252 - 0.268	Pl ± opx ± amp Pl ± opx ± amp ± (biot)	52-66	1.8-3.2
Nocarane	>640 - 808	175-200?	65.53-125.93	0.350 - 0.673	Pl ± cpx ± ol Pl ± amph ± cpx Pl ± amph ± bi	55-66	1.8-4.2
Chingana	916* - 1100?	80-100	32.10-47.40	0.356 - 0.526	Pl ± cpx ± ol Pl ± opx ± cpx ± amph	59-60	1.8-2.8
Chachani base	1100 – 1278	100-200	1.33-3.62	0.009 - 0.024	Pl ± cpx ± (opx)	59-61	2.8-3.2

Table 3. Summary of growth stages, eruptive rates, mineral assemblages, and $Si0_2$, K_20 content in lavas from the C-LVC.

Name	Min. age (ka)	Max. age (ka)	Observations	Estimated duration (ka)	Min. vol km^3	Max. vol km^3	Eruption rate km^3/ka	Comments	Rounded rate km^3/ka
'Young' edifices									
Volcancillo	50?	150?	Un-glaciated dome in wide crater	< 50? (short lived)	0.33	0.39	0.006-0.007	likely shorter	0.006-0.01
Cabreria	56.5	< 130	Dome collapse block-and-ash flows	50 ?	4.13	4.91	0.082-0.098		0.08 - 0.10
Chachani	130 middle	222 base	Top not dated, craters preserved	90 - 130 max	30.34	33.20	0.275-0.302		0.27-0.31
Uyupampa	231	250?	Voluminous lava field	50 - 100?	2.36	2.72	0.031-0.036	likely shorter	0.03-0.04
El Rodado	239	< 400	Base not dated	200	6.26	9.17	0.031-0.045	likely shorter	0.03 - 0.05
La Horqueta	332	< 400	Older than Airport domes	100	3.24	6.46	0.032-0.064	likely shorter	0.03 - 0.07
Potrero domes	291	397	Dome cluster, short growth	100	11.22	12.53	0.112-0.125	likely shorter	0.11 - 0.13
El Angel	~400	463	Top not dated, crater preserved	60 – 100?	4.86	5.56	0.060-0.069	likely shorter	0.06 - 0.07
				'Young' Edifices	**63 ± 6.3**	**75 ± 7.5**	**Young volcano typical average eruption rate**		0.07 - 0.09
	< 640 Temporal gap > 463?						**Estimated eruption rate over 500 kyr**		**0.12 - 0.15**
'Old' edifices									
El Colorado	640	642	Two dome coulees	< 50 (short lived)?	4.13	6.16	0.082 - 0.123	likely shorter	0.08 - 0.13
Estribo	694	< 916	Overlies 1.4 Ma PDC (top IAI unit)	220 - 250?	59.35	63.03	0.252 - 0.268	likely longer	0.25 - 0.27
Nocarane	> 640	916	Top not dated; deeply eroded	175 - 200?	65.53	125.93	0.350 - 0.673	likely longer	0.35 - 0.70
Chingana	916 middle	1012	Top not dated; deeply eroded	80 - 100?	32.10	47.40	0.356 - 0.526	likely longer	0.35 - 0.60
C-LVC base	1012	1278 (Yura Tuff)	Lava flows	100 - 200	1.33	3.62	0.009 - 0.024	likely shorter	0.01 - 0.03
				'Old' Edifices	162 ± 16	246 ± 24	**Old volcano typical average eruption rate**		0.21 - 0.34
							Estimated eruption rate over 600 kyr		0.27 - 0.41
			Entire C-LVC volume		290 ± 29	350 ± 35	**Eruption rate over 1100 kyr**		0.26-0.31

Table 4. Results of calculation using morphometric parameters for the C-LVC and each of its edifices.

EDIFICE	ROCK TYPE	MAIN TEXTURE	MINERAL ASSEMBLAGE			OBSERVATIONS
			Crystal max. size	Pheno- and microphenocryst	Microlite in groundmass	
Pre-Chachani	Andesite	Microporph. Glomeroporph. vesiculated	2 mm	pl±cpx±(opx) (~23 %)	pl±cpx±mgt (~20%)	~10 % of vesicles. pl: sieve and overgrowth opx, cpx: dissolution surfaces
'OLD' EDIFICES GROUP						
Chachani Base	Andesite	Microporph.	2-4 mm	pl±cpx±amph pl±amp±bi (28-34%)	pl±cpx (30-34%)	sieve: pl patchy zoning: cpx breakdown: cpx, amph, rare ol
Chingana	Basaltic andesite	Microporph.	1 mm	pl±cpx±ol (~38 %)	pl±cpx±ol (~30 %)	intergrowth: plg-cpx sieve: pl; resorption: cpx, opx, pl, amph, ol
	Andesite	Microporph.	1-3 mm	pl±opx±cpx±amph (32-33%)	pl (26-30%)	2 types of pl; dissolution: pl, cpx intergrowth: pl-amph
Nocarane	Basaltic andesite	Porphyritic, glomeroporphyric	2 mm	pl±cpx±ol plg±opx±ol (aggregates)-(~21 %)	pl±cpx±ol (~31 %)	sieve: pl resorption: pl, cpx, opx
	Andesite	Porphyritic, poikilitic	4 mm	pl±amph±cpx (22-34 %)	pl±(cpx) (16-31%)	sieve: pl dissolution surf.: opx, cpx
	Dacite	Porphyritic	5 mm	pl±amph±bi (~24 %)	pl±(mgt) (~31%)	resorption: amph
Estribo	Dacite	Aphanitic, porphyritic	4 mm	plg±opx±amp (~22 %)	plg±px (~37%)	resorption: pl breakdown: opx intergrowth: pl et opx.
	Andesite	Vitrophyric, glomeroporphyric	5 mm	pl±cpx±amp (6-36%)	pl±mgt (21-61%)	sieve: pl breakdown: amph dissolution: bi
El Colorado	Andesite	Porphyritic, spherulitic	4 mm	plg±amp±bi (29-37 %)	pl±mgt (~12%)	devitrification of glass sieve and skeletal: pl patchy zoning: amph
'YOUNG' EDIFICES GROUP						
El Angel	Andesite	Porphyritic	6 mm	pl±amp±cpx±(biot) (~31%)	plg±cpx±oxy (~45%)	sieve, skeletal and overgrowth in pl; resorption: amph
El Rodado	Andesite	Porphyritic	2-6 mm	pl±cpx±(ol) (15-40%)	pl±cpx±(mgt) (26-52%)	sieve: pl breakdown: amph, rare ol.
La Horqueta	Andesite	Porphyritic	3-7 mm	pl±amp±bi±(cpx) pl±cpx±amph (30-45 %)	pl±amp±cpx±(mgt) (18-31 %)	sieve and dissolution: pl breakdown: amph, cpx, ol
Potrero Domes	Andesite	Porphyritic	4-6 mm	pl±amp±cpx±biot (~25 %)	plg±cpx (~46 %)	sieve: pl overgrowth: pl resorption: pl, cpx
	Dacite	Porphyritic	5-9 mm	pl±amp±(cpx) (24-39 %)	pl±px (29-49%)	sieve: pl, intergrowth: pl-amph resorption: px and bi breakdown: amph, bi
Uyupampa	Andesite	Porphyritic	3-5 mm	pl±amp±bi (30-42%)	pl±cpx±(ol) (20-43%)	sieve, overgrowth in pl

						resorption and breakdown in amph
Chachani	Dacite	Porphyritic	3-5 mm	pl±opx±amp±(biot)	pl±opx	resorption: pl, opx breakdown: amph
	Andesite	Porphyritic	3-5 mm	pl±amp±px (31-41 %)	pl±opx (20-50%)	sieve: pl dissolution: pl, amph, px breakdown: amph
La torta	Andesite	Porphyritic	6 mm	pl±px±ol±bi (~41 %)	Pl±px (~17 %)	dissolution: pl, bi, cpx breakdown: amph
Cabreria domes	Andesite	Aphyric	5 mm	Pl (~13 %)	pl±px (~15 %)	sieve: pl breakdown: amph
Volcancillo	Dacite	Porphyritic	5 mm	pl±amp±bi (~45 %)	pl±amp±px (~18 %)	sieve: pl resorption: pl and bi breakdown: bi

Table 5. Petrographic characteristics of lavas from the twelve C-LVC edifices, and of Pre-Chachani and Chachani base lavas. Pl: plagioclase, opx: orthopyroxene, cpx: clinopyroxene, amph: amphibole, bi: biotite, mgt: magnetite. % values in parentheses represents the percentage of crystal content as phenocrysts (>500 μm) and microphenocrysts (100-500 μm) and microlites (<100 μm) in the groundmass.